JGR Atmospheres

RESEARCH ARTICLE
10.1029/2023JD038754

A "Boreing" Night of Observations of the Upper Mesosphere and Lower Thermosphere Over the Andes Lidar Observatory

J. H. Hecht[1], A. Z. Liu[2], D. C. Fritts[3], R. L. Walterscheid[2], L. J. Gelinas[1], and R. J. Rudy[1,4]

[1]Space Science Applications Laboratory, The Aerospace Corporation, El Segundo, CA, USA, [2]Embry-Riddle Aeronautical University, Daytona Beach, FL, USA, [3]GATS, Boulder, CO, USA, [4]Kookoosint Scientific, Camarillo, CA, USA

Key Points:

- High-spatial resolution observations captured a mesospheric bore with a distinct leading phase
- These observations also captured clear evidence of instabilities driving bore dissipation
- Bore dissipation caused a significant momentum flux divergence and mean wind acceleration within the duct

Supporting Information:

Supporting Information may be found in the online version of this article.

Correspondence to:

J. H. Hecht,
james.hecht@aero.org

Citation:

Hecht, J. H., Liu, A. Z., Fritts, D. C., Walterscheid, R. L., Gelinas, L. J., & Rudy, R. J. (2023). A "boreing" night of observations of the upper mesosphere and lower thermosphere over the Andes Lidar Observatory. *Journal of Geophysical Research: Atmospheres*, *128*, e2023JD038754. https://doi.org/10.1029/2023JD038754

Received 22 FEB 2023
Accepted 12 SEP 2023

Author Contributions:

Formal analysis: J. H. Hecht, A. Z. Liu, R. L. Walterscheid
Investigation: J. H. Hecht, A. Z. Liu, D. C. Fritts, R. L. Walterscheid, L. J. Gelinas, R. J. Rudy
Methodology: A. Z. Liu, D. C. Fritts, R. L. Walterscheid
Writing – original draft: J. H. Hecht
Writing – review & editing: J. H. Hecht, A. Z. Liu, D. C. Fritts, R. L. Walterscheid, L. J. Gelinas, R. J. Rudy

Abstract A very high-spatial resolution (~21–23 m pixel at 85 km altitude) OH airglow imager at the Andes Lidar Observatory at Cerro Pachón, Chile observed considerable ducted wave activity on the night of 29–30 October 2016. This instrument was collocated with a Na wind-temperature lidar that provided data revealing the occurrence of strong ducts. A large field of view OH and greenline airglow imager showed waves present over a vertical extent consistent with the altitudes of the ducting features identified in the lidar profiles. While waves that appeared to be ducted were seen in all imagers throughout the observation interval, the wave train seen in the OH images at earlier times had a distinct leading nonsinusoidal phase followed by several, lower-amplitude, more sinusoidal phases, suggesting a likely bore. The leading phase exhibited significant dissipation via small-scale secondary instabilities suggesting vortex rings that progressed rapidly to smaller scales and turbulence (the latter not fully resolved) thereafter. The motions of these small-scale features were consistent with their location in the duct at or below ~83–84 km. Bore dissipation caused a momentum flux divergence and a local acceleration of the mean flow within the duct along the direction of the initial bore propagation. A number of these features are consistent with mesospheric bores observed or modeled in previous studies.

Plain Language Summary Images taken on the night of 29–30 October 2016 from a high-spatial resolution OH airglow camera and simultaneous data from a Na wind-temperature lidar, colocated at the Andes Lidar Observatory on Cerro Pachón, Chile, revealed the presence of a mesospheric bore. The bore was located in a ducted region formed by large temperature and wind gradients present in the 82–88 km altitude region. Such bores in the atmosphere, that appear as a moving wave, are analogous to bores that form in river channels. Many of the observed features of this atmospheric bore are consistent with previous observations and modeling. However, these new data also showed, at the very high-spatial resolution that are unique to these images, that the bore dissipated, forming turbulent-like features and causing a momentum flux divergence within a duct that accelerated the mean wind along the direction of the bore propagation.

1. Introduction

During the Airborne Lidar and Observations of the Hawaiian Airglow (ALOHA) 1993 campaign Taylor et al. (1995), hereafter T95, observed an unusual wave-like event in OH airglow emission images originating at a nominal altitude of ~85 km. The event consisted of a series of wave phases where the first phase had a steep leading edge that was followed by smaller amplitude wave phases thereafter. Their observations also included images from a second airglow emission feature, the O_2A (O_2 atmospheric) band originating above ~90 km. In those images, the O_2A wave amplitudes had an inverse relationship with the amplitudes of the OH emission layer waves. Based on those characteristics Dewan and Picard (1998), hereafter DP98, suggested, by analogy with bores that develop from hydraulic jumps in river channels (Lighthill, 1978), that these unusual images were manifestations of mesospheric bores. Following this analogy, DP98 argued that a temperature inversion layer serves as a duct for atmospheric gravity waves (AGWs) that obey the AGW dispersion relation, and for their nonlinear manifestations referred to as mesospheric bores. DP98 also identified analogous quantities in the mesosphere to those used to derive the equations for river bores. Using this approach and expanding on the details in a subsequent paper Dewan and Picard (2001), hereafter DP01, were able to provide a plausible explanation of the T95 observations and suggested criteria for identifying mesospheric bores. These observational and theoretical efforts stimulated significant studies, both observational and modeling, and many references to such work can be found in the recent paper describing mesospheric bore observations using polar mesospheric cloud (PMC) imagery (Fritts et al., 2020).

While DP98 and DP01 provided a basis for the existence and character of mesospheric bores, more rigorous modeling analyses were performed by Seyler (2005) and Laughman et al. (2009, 2011). These authors showed that given a duct (thermal and/or Doppler) a trapped AGW could evolve, nonlinearly, into an approximately solitary wave that are idealized solutions of approximate nonlinear equations intended to provide insights into such motions in geophysical fluids. The nonlinear wave is not purely sinusoidal and has a steep (slightly shortened horizontal-wavelength) leading edge. This leading wave can be followed by smaller amplitude more sinusoidal-shaped trapped waves. These modeling efforts revealed a number of features that resemble the T95 observations and provided approximate criteria for identifying bores or bore-like features in airglow imagery.

Subsequent to the original T95 bore imagery, multiple efforts were made to identify bores in airglow imagery and to use multi-instrument diagnostics and modeling to identify the atmospheric conditions present, and specifically to explore the presence and character of the duct (e.g., Nielsen et al., 2006; She et al., 2004; Smith et al., 2003, 2005, 2017; Stockwell et al., 2011; Walterscheid et al., 2012; Yue et al., 2010). While some of these studies (e.g., Walterscheid et al., 2012), showed imagery in multiple channels that are quite similar to the original T95 observations, a number of the cited studies revealed quite disparate character. What complicates the interpretation of the bore observations is that both ducted wave fronts and large wall waves (Swenson et al., 1998) exhibit wave imagery that resembles bores. This is discussed in Smith (2014). The difficulty in understanding the relation of bore to wall wave imagery was also noted by Shiokawa et al. (2006) whose imagery suggested a bore response but they could not identify the presence of a duct. Also, Hecht et al. (1995) using data from the same ALOHA 1993 campaign, but on different nights then when the Taylor et al. (1995) bore and the Swenson et al. (1998) wall waves were observed, noted that sudden large jumps in airglow intensity, that could resemble a bore could also be due to downwelling of atomic oxygen during large AGW activity. More details about this interesting event are found in the cited references.

One question about the lifecycle of a mesospheric bore that has been partially, but not unequivocally, addressed is the dissipation of the bore. She et al. (2004) seem to have been the first to address this with multi-instrument diagnostics from which they inferred a decaying bore, but the low resolution of the imagery precluded a definitive conclusion. Stockwell et al. (2011) performed an extensive analysis of the observations by Nielsen et al. (2006), where the bore appeared to fade but with no obvious decay into turbulence. More recently, there have been at least two studies that observed some of the instability features Hecht (2004) associated with the breakdown of AGWs in airglow imagery. Medeiros et al. (2018) described a case study of a bore dissipation where there were observations small horizontal-scale features aligned perpendicular to the bore phase, sometimes called ripples, that would suggest the presence of an instability based on Hecht (2004). However, the exact correspondence between the ripples and the bore decay was unclear. Similarly, Mondal et al. (2021) observed a bore that appeared to dissipate at a time when ripples appeared. In this case, the authors used satellite and model data to infer that a duct was present. Again though, the exact relation of the bore phase to the ripples was not clear.

Finally, Fritts et al. (2020), hereafter F20, used PMC imaging to observe two separate wave-like features they identified as mesospheric bores. PMC imaging has the advantage of being able to observe very fine structure at better than 100 m scale size, a resolution that is only currently matched by the airglow imagery in this study. The disadvantages of PMC imaging are (a) that only a restricted altitude range of a few km can be observed and (b) because PMCs can be discontinuous, some aspects of the bore propagation/evolution may not be revealed. However, the PMC Turbo campaign instrumentation also included a Rayleigh lidar that allowed temperature retrievals below the PMCs and tracking of advecting features within the PMC bore response. The atmospheric environments at the PMC altitudes were complex with the bores apparently being forced by associated AGWs. Instabilities were associated with the forcing, but these are distinct from the subsequent instabilities accompanying bore dissipation. Most of the discussion in this study addressed understanding the formation and evolution of the bores and of their observed instabilities. There is also some discussion of their Figure 10, relevant to the current study, that shows small-scale instabilities accompanying the leading bore phase.

Hence, while there has been significant research on the formation, evolution, and dissipation of bores, there remains a lack of high-resolution, multi-instrument observations of the evolution and dissipation of mesospheric bores in known environments. Because bores often evolve a distinct nonlinear large amplitude wave with a steep leading edge, we might expect large temperature gradients at these locations and potential instabilities such as those identified by F20. This would cause dissipation and limit the bore lifetime. However, previous bore observations have often lacked the environmental measurements enabling further quantification of these dynamics.

Multi-instrument ground-based observatories, such as the Andes Lidar Observatory (ALO) (30.25°S, 70.73°W, 2,530 m) at Cerro Pachón in northern Chile, which houses airglow imagers and a Na resonance lidar, are ideal for detailed studies of phenomena such as bores, AGWs, and instability dissipation, providing such an event occurs over the observatories field of view (FOV). ALO studies of AGW and instability dissipation have recently been reported (Fritts et al., 2014, 2021; Hecht et al., 2014, 2018, 2021).

On the night of 29–30 October 2016, immediately following instrument turn-on after sunset, an apparent bore (with no instability features) was present in high-spatial resolution OH imagery. These images had ∼25 m pixel resolution sufficient to detail the formation of instabilities. A separate all-sky two channel airglow imager (OH and greenline) revealed the bore to be present in only the OH channel. Lidar wind and temperature data revealed the presence of a duct, for waves propagating with the observed direction and velocity, only in the OH emission layer. The dissipation of the bore was observed and included fine ripple structure and vortex rings, apparently associated with the steep leading phase front of the bore. After the bore dissipated apparent ducted waves were seen that were roughly perpendicular to the previous orientation of the bore phases and persisted to sunrise, with no additional bore formation during this latter interval.

This paper describes these observations of the dissipation of an apparent bore and is structured as follows. Section 2 describes the ALO instrumentation and analysis methods. The lidar and airglow observations are described in detail in Section 3. Section 4 provides a discussion of the observations and a comparison with previous studies. A summary of these dynamics and their potential implications is provided in Section 5.

2. Experimental Technique

2.1. Instrumentation at the Andes Lidar Observatory (ALO)

Observations discussed here were carried out at ALO in north-central Chile. Some of the instruments below were discussed in Hecht et al. (2021) that provides additional details.

2.1.1. ANI2 (Aerospace Nightglow Imager 2)

The main instrument for this study is The Aerospace Corporation's second version near-IR camera, the Aerospace Nightglow Imager 2 (ANI2), which images the OH airglow. This is accomplished by imaging through an H-band filter centered near a wavelength of 1,600 nm onto a Teledyne model H2RG HgCdTe focal plane array (FPA), which has 2,048 × 2,048 pixels, each with 18 μm on a side. The FOV from edge to edge of the FPA is just under 30°. For observations at 85-km altitude above mean sea level, which is representative of this study, the center, edge, and corner pixels have a footprint of 20.6, 22.6, and 24.8 m, respectively. Note that ALO is at about 2.5-km altitude so that 85 km is only 82.5 km above ALO. Except where noted, the images are binned 2 × 2 resulting in an effective pixel footprint at 85 km of between 41.2 and 45.6 m over the FOV. The center pixel is 1.7° west and 2.0° south of zenith, and the entire image is rotated 2.3° clockwise with respect to the geographic north south line. In all these images, east is on the left and north is on top. This is the equivalent of viewing the sky looking up from the ground and is consistent with the orientation of these imagers in past studies. However, to be consistent with typical conventions, we arbitrarily denote 0° as north and 90° as east even though in the ANI2 images this means degrees increase in the counter clockwise direction. The reader is referred to Hecht et al. (2021) for a more detailed description of the image orientation.

For this study, two frames are typically taken for each observation with an integration time of 1.475 s for the first frame, designated as number one, and 2.95 s or larger for the second frame, designated as number 2. There are two different reduction algorithms that are used in this study. For the difference-frame results, two consecutive number 2 images (separated by nominally 60–75 s) are subtracted. For the all-frame results, a fixed number 2 image with little structure (at the end of the night) is chosen and subtracted. All these subtractions are needed to remove the static chip structure that would otherwise be present in an image. More discussion of this is given in Hecht et al. (2021). As noted in that study the difference-frame technique (hereafter diff-mode) provides better contrast of the instability features but causes some complexity in identifying them. The all-frame technique (hereafter all-mode) eliminates that uncertainty but does not provide as high a contrast of the small-scale instability features.

2.1.2. University of Illinois at Urbana-Champaign/Embry-Riddle Aeronautical University (UIUC/ERAU) All-Sky Camera

The all-sky camera has a 180° FOV for both of its airglow channels. One channel images the OH (6, 2) band that occurs mainly below 90 km, while the other channel images the OI(557.7 nm) greenline emission that occurs

near 95 km. Images are taken every 60 s for OH, and 90 s for OI, and the pixel FOV is ~550 m at the center of the image (Vargas et al., 2020). Historically, these images have been presented as if one is viewing the sky from above and thus east (90°) is to the right when north (0°) is on top. This is opposite the convention that the Aerospace imagers and auroral all-sky cameras have used. A comparison between these orientations will be shown later.

2.1.3. University of Illinois at Urbana-Champaign/Embry-Riddle Aeronautical University (UIUC/ERAU) Na Resonance Lidar

The UIUC/ERAU Na Lidar provides vertical and slant profiles of wind, temperature, and Na density at high vertical (500 m) and temporal (60 s) resolutions. The two horizontal components of the wind vector were calculated from the line-of-sight (LOS) wind measured when the lidar beam was pointed to 20° off-zenith toward the south (S) or the east (E). The vertical component is the LOS wind when the lidar beam was pointed to zenith (Z). The beam was pointed to these three directions in the sequence ZEZS with a 60 s dwell time in each direction. The horizontal wind was derived from the off-zenith LOS wind as described in Liu et al. (2002). They were then smoothed with a 15 min full-width Hamming window in time at 6 min and 500-m intervals. As discussed in Hecht et al. (2021), the east and south wind measurements occur slightly outside the FOV of ANI2. At 6 min and 500-m intervals, the LOS wind and temperature errors are about 6 m/s and 1 K, respectively, in the 88–89-km altitude range. These errors are larger at 85 km and below and at 95 km and above. During the main period of interest around 0 hr UT, the LOS wind error at 82.5 km is about 8–9 m/s.

In this work, the lidar data are used primarily to determine the vertical wavenumber, m, discussed in the next section, from which altitude regions can be determined where AGWs are either freely propagating or evanescent. Thus, the locations of potential AGWs and/or bore ducts can be identified.

These data can also be used to assess the stability of atmospheric regions via the Richardson number, $\mathrm{Ri} = N^2/(du_h/dz)^2$ (Richardson & Shaw, 1920). Here, N is the Brunt-Vaisala frequency and du_h/dz is the vertical shear of the horizontal wind. As noted in the extended discussions of instability formation by many authors spanning decades, when $\mathrm{Ri} < 0.25$ an enhanced shear layer enables formation of Kelvin-Helmholtz instabilities (KHIs), resulting in responses referred to as "ripples" in previous airglow observations as discussed, e.g., in Hecht (2004). Other instabilities can arise for $\mathrm{Ri} > 0.25$ accompanying parametric instabilities (e.g., Sonmor & Klaassen, 1997; Walterscheid et al., 2013). When the atmosphere starts to overturn and becomes convectively unstable ($\mathrm{Ri} < 0$) it had been suggested that additional instabilities may occur (Fritts et al., 1997; Hecht, 2004; Hecht et al., 1997), but more recent modeling suggests that even before overturning occurs AGWs can become unstable (e.g., Fritts et al., 2009a). Importantly, AGWs exhibit "breaking" via vortex ring formation for amplitudes above and below overturning (Fritts et al., 2009b), and even weak AGWs in multiscale environments can induce small-scale KHI on thin sheets having large N^2, but induced $\mathrm{Ri} < 0.25$ (Fritts et al., 2016). Thus, caution is required in characterizing specific instability dynamics in the presence of AGWs.

2.1.4. AGW Wavenumber Using Lidar and Imager Data

As noted above, AGWs can be trapped in a duct and evolve nonlinearly into a bore that could include a leading solitary wave structure with a steep leading edge and amplitude-ordered trailing phases. The nonlinear aspects of the evolution of an AGW into a bore were analyzed in detail first by Seyler (2005) and then by Laughman et al. (2011) using several approaches. These included an approach that used the small-amplitude nonlinear Benjamin-Davis-Acrivos-Ono (BDAO or sometimes denoted BDO) model equations (e.g., Benjamin, 1967; Laughman et al., 2011).

This study uses a linearized AGW dispersion relation for the vertical wavenumber, m, in order to determine whether a duct could exist for an AGW traveling in the direction of the wave velocity. Note that a number of studies have found using linear dispersion relations useful in studying the ducted nature of bores (Laughman et al., 2011; Walterscheid & Hickey, 2009; Walterscheid et al., 2012). Moreover, the difference between a linearized approach and a nonlinearized approach, which is beyond the scope of this work, is likely to be less than the observation uncertainties discussed later.

We consider the following dispersion relation, shown in Equation 1, that is derived assuming isothermal conditions, but may be applied to nonisothermal conditions when m varies slowly over a wavelength (Einaudi & Hines, 1970; Fritts & Alexander, 2003; Hecht, 2004). This is the dispersion relation that has been used in many of our previous studies discussed in Section 1 with a few differences that account for the fact that for AGWs

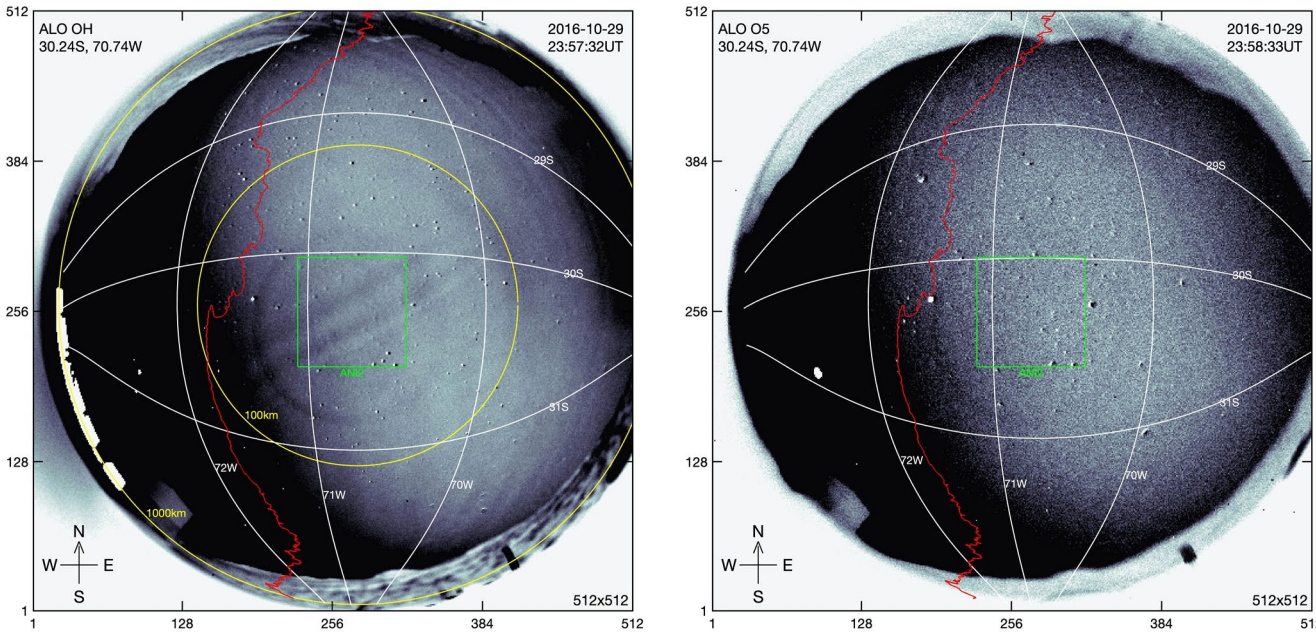

Figure 1. (left) OH all-sky difference image at 2357 UT on 29 October 2016. Positions for the ANI2 FOV, radial lines at 100 and 1,000 km (projected to 85 km altitude), lines of latitude and the Chilean coastline are all shown. (right) Greenline difference image. The radial lines are not shown on this image and the ANI2 FOV is projected to 96 km, the nominal altitude of the greenline. Note, however, ANI2 only observes in the OH emission band.

observed in these images many of the terms are quite minor. This dispersion relation was also found to have no appreciable difference in the determination of regions where m is real or imaginary compared to the equations used in the references above

$$m^2 = \frac{N^2k^2}{\omega_I^2} - k^2 = \frac{N^2}{c_I^2} - k^2 \tag{1}$$

In Equation 1 ω_I is the intrinsic frequency, which is the frequency measured in the frame of reference that moves with the background wind, and k is the horizontal wavenumber equal to $2\pi/\lambda$ where λ is the horizontal wavelength. For a given background mean wind velocity component, $\bar{u}$, in the direction of wave propagation, and an observed wave horizontal phase velocity, c, the intrinsic wave phase velocity, c_I, is given by $c - \bar{u}$ which is equal to ω_I/k.

3. Results

This section employs ALO all-sky and ANI2 airglow imaging, and relevant lidar data to describe and interpret the features seen to accompany the bore event occurring on 29–30 October 2016. Movies of the airglow imaging that reveal additional details of these dynamics are included in Supporting Information S1.

3.1. Overview From the All-Sky Imager Movies for the Entire Evening

Two movies labeled in Supporting Information as Movie S1 (for OH imagery) and Movie S2 (for greenline imagery) provide ~1 min (for OH) and 1.5 min for greenline difference imaging from just after sunset to almost sunrise, a longer data period than for any of the other instruments. The main purpose of presenting these movies is to determine if the bore feature is isolated in one of the airglow emission channels, thus constraining its altitude location.

To help the reader, the most significant frames of the OH and greenline movies, at 2357 and 2358 UT on 29 October, respectively, are shown in Figure 1. In the OH image, the ANI2 FOV is shown as well as radial distances, projected to 85 km altitude, of 100 and 1,000 km, lines of latitude and longitude, and the Chilean coastline. The 85 km altitude region is within the nominal OH emission region that ANI2 also observes. In the greenline image, the ANI2 FOV is shown projected to 96 km and this helps the reader determine the wave activity in the greenline

layer compared to the OH observations. Both FOVs have some slight distortion (not corrected for) and thus the ANI2 FOV is drawn as a perfect square even though it is slightly warped by a few percent. The placement of the ANI2 FOV was determined by the star field (that can be different in the visible and near-IR) and the location of the phase fronts seen also in the ANI2 imagery at that time. We remind the reader that the all-sky lens also has inherent distortion and is not linear. These frames are taken about ∼16 min after the ANI2 imager turned on. The key result is that, in these frame, the greenline image shows no wave phases in the center of the FOV, while the OH image shows three wave phases aligned perpendicular to a line running from roughly Northwest (NW) to Southeast (SE). This localizes these wave phases to the altitude of the OH layer.

These waves in the OH movie persist for about 30 min but are quickly overwhelmed by a bright wave train originating from the Southwest (SW) and moving toward the Northeast (NE). Waves propagating in this direction are present much of the time for the remainder of the night. These waves are not continuous though, and are less continuous from ∼4 to 8 UT. After 8 UT, a distinct new front of small-scale wave phases appear (from the same direction) and those waves are present at sunrise. There are also periods where waves propagate in other directions. Movie S2 looks similar to the Movie S1 much of the time with the exception following turn-on that was noted above.

3.2. Observations of an Apparent Bore

The focus of this study is on the apparent bore event that occurred from 234407 (hhmmss) UT to 002729 UT, the interval shown in Movies S1 and S2 that end when the bore dissipation seems complete. These movies are briefly discussed in the next section; thereafter we provide a more detailed discussion of the bore phase evolutions using individual frames. Note again that during this interval in the all-sky movies three wave phases are seen in Movie S1 and none in Movie S2.

3.2.1. Overview From the ANI2 Imager Movies for the Entire Evening

Two additional movies labeled Movie S3 or ALL1 (for all-mode ANI2 imagery) and Movie S4 or DIFF1 (for diff-mode ANI2 imagery) are provided in Supporting Information S1. The first frame of Movie S3 shows a prominent wave phase aligned from the upper left (NE) corner to the middle of the right edge (W). A portion of a second wave phase is seen in the upper right (NW) corner. To the SE of the first wave phase, there are some possible wave-like features but there are no obvious areas of turbulence or other instability features that have been identified in previous studies discussed in Section 1 (e.g., Hecht et al., 2018, 2021). This leading wave phase propagates to the SW and as it advances features aligned perpendicular to it appear (e.g., frame 48 of ALL1). The leading edge of the leading wave phase appears more sharply defined and steeper than the leading edges of the trailing wave phases. Irregular, apparently turbulent features also appear ahead in front of the leading wave phase, some of which resemble vortex rings as seen leading and/or trailing the various bore phases described by F20, and which accompany more general AGW breaking (e.g., Fritts et al., 2017; Hecht et al., 2018). These features appear to be mostly advected to the right (W) although they also exhibit some motion toward the bottom (S). As time advances, the leading wave phase appears to dissipate and trailing wave phases appear and propagate toward the SE where they also begin to dissipate. The wave phases appear to dissipate over about 10–15 km in distance and over about 10–15 min per phase. This wave train that has a prominent leading phase resembles a mesospheric bore, and their phases will be referred to hereafter as bore phases.

After about 001000 UT, additional wave-like phase features appear to propagate roughly perpendicular to the direction of propagation of the bore phases. An examination of the movie frames after 004000 shows that these wave-like motions are now largely from the SW to NE, a direction nearly perpendicular to that of the bore phases. These will be discussed only briefly later in this discussion.

The DIFF1 movie accentuates departures from sinusoidal brightness variations because the bore phases advance only ∼1/8th of the bore wavelengths over the 1-min difference period. This causes the majority of the bore phase brightness variations to be attenuated, although the leading steep nonsinusoidal phase remains visible. In particular, nonsinusoidal brightness variations evident in these difference images are of two types. Larger-scale brightness variations that are coherent along the bore phases reveal that the bore brightness is not purely sinusoidal, as seen at the leading edge of the leading bore phase. Such a nonsinusoidal variation is consistent with a class of idealized bores as noted above. Embedded smaller-scale features that are revealed more clearly than in the undifferenced imaging are evidence of instabilities accompanying the bore evolution. Several examples of these responses are described in greater detail below.

3.2.2. Bore Features and Scales From Frames Extracted From Each ANI2 Movie

While the ANI2 movies show the evolution of the bore event, selected frames, shown in Figure 2, enable a more detailed discussion of their evolving features. The rows show derived image results from frame 16 (234708 UT) in the top row, frame 40 (235110 UT) in the middle row, and frame 68 (235554 UT) in the bottom row. The columns are as follows. The left column presents diff-mode images and they all show an added black diagonal line from the upper left NE to the SW along or parallel to a bore phase crest. The location of this line is the same in all of these images. The right column shows the corresponding images in the all-mode with the same diagonal line parallel to the bore phase. In addition, these all-mode images have added black and white diagonal lines from the SE to the NW, essentially perpendicular to the bore phase crests. The black lines start at the upper right (NW) corner while the beginning position of the white line varies. For frame 16, this line starts at pixel 150 (with pixel 0 in the upper right corner) while it starts at pixel 250 in the other two frames. Plots of these lines are shown in succeeding figures.

Before discussing these line plots, shown in Figure 3, we present an overview of the images shown in Figure 2. In the top image of the right column the leading bore phase, which has the black diagonal line along the crest, appears to have a clear nonsinusoidal leading phase. A close examination of this panel also reveals faint, thin line-like features perpendicular to the bore phase, reminiscent of the secondary convective instabilities that have been seen in imaging to appear perpendicular to AGWs that are associated with overturning (Hecht, 2004; Hecht et al., 1997), or in KHIs at smaller scales as they start to dissipate and form secondary convective instabilities (Hecht et al., 2014). As the bore progresses toward the SE, as shown in the middle and lower panels of the left column, the leading bore phase distorts and becomes slightly curved, the perpendicular features become more noticeable, and turbulent-like features associated with AGW breakdown, such as vortex rings as discussed below, appear at the leading edge of the leading bore phase (e.g., Fritts et al., 2017; Hecht et al., 2018). The 1-min diff-mode images, shown in the left column, support this analysis. As noted earlier, the image differencing almost eliminates the leading bore phase, but does not eliminate the steep leading edge. The region around this edge evolves over the three frames (from the top to the bottom images) to show more turbulent-like structures, suggesting the breakdown of the bore.

Figure 3 shows line plots for the white (left column) and black (right column) diagonal lines, that are perpendicular to the crests of the bore phases. These line plots allow a measure of the morphology of the bore phases. It is apparent that the leading bore phase (with a peak at pixel numbers 500–600) has a larger amplitude over the background than the trailing bore phases. In fact, the right panels, which show plots of the black diagonal lines, show a decrease in amplitude for the trailing bore phases. The differences between the leading and trailing bore phases are further explored in the left panels with the white diagonal line plots. In the top panel, the leading and trailing bore phases have green and red over-plots, respectively. These are sinusoidal fits to the shape of the observed bore phases. While the red over-plot fairly matches the observed shape of the trailing phases, the green over-plot indicates that the leading edge of the leading bore phase is steeper than is found in a sinusoidal profile. This becomes even more apparent in the middle and lower panels. It also appears that the leading bore phase may have a flatter peaked region. A nonsinusoidal profile with a steep leading phase front is as noted before characteristic of a bore.

The imagery and plots from Figures 2 and 3 also allow estimates of the observed phase speed and wavelengths of the bore. The observed period of 526 s was taken from the motion of a wave phase between frames 16 and 68. The horizontal wavelength was taken as the difference between the first two peaks (minima) in the upper (middle) left (right) panel of Figure 3. The number of binned vertical pixels (shown on the axis) between the peaks is about 290. Given the approximate angle of the wave phase of 28.3° and a 42.5 m binned pixel we obtain an estimated wavelength of 14.0 km and a phase velocity of ∼26.6 m/s.

Finally, these plots can also be used to estimate the fractional airglow perturbation, induced by the bore, if the absolute airglow intensity is known. The absolute airglow intensity can be found by subtracting the corresponding number 1 image from the number 2 image. While all the focal plane array structure is not removed, the mean airglow intensity in counts is easily obtained and yields a fractional perturbation amplitude of the leading bore phase of ∼0.06. This number will be used later in the analysis.

3.2.3. Fine-Scale Features and Apparent Instabilities Associate With the Bore Phases

Figure 4 shows line plots of the diagonal lines along approximately on, or parallel to, the crest of the bore phases, in both the all-mode (right column of Figure 2) and diff-mode (left column of Figure 2) images for the three frames. The all-mode data (shown in the right column of this figure) show evidence of fine structure on top of some larger oscillations along the bore phase crest. Note that the line for middle panel of each column (frame 40)

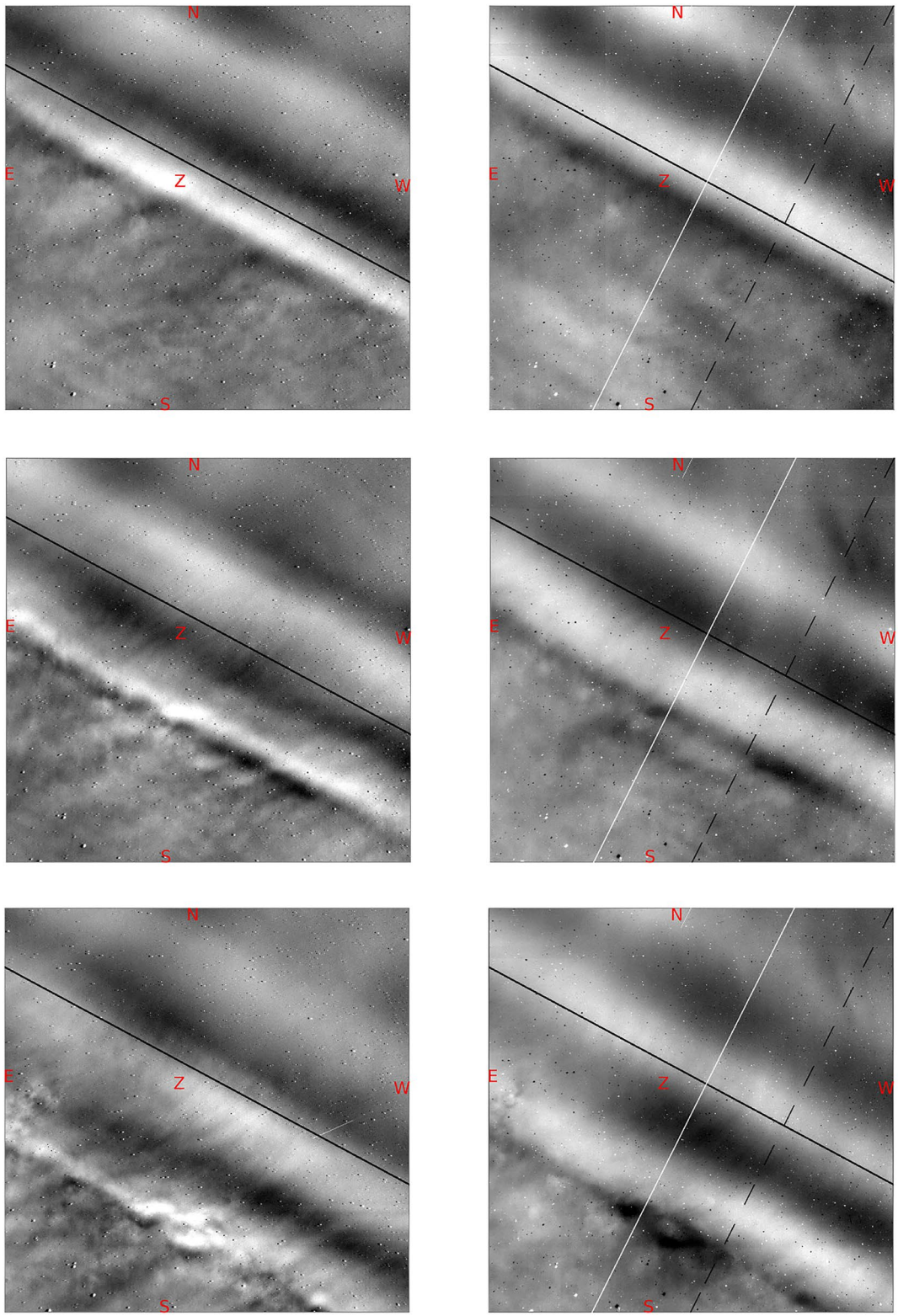

Figure 2.

is actually at a minimum while for the other two panels the lines traverse along the maximum intensity (the crest) of the bore phase. The all-mode images suggest that there may be faint wave-like features, separated by well over 10 km, perpendicular to the leading bore phase. This would be consistent with the almost constant propagation of waves perpendicular to the bore throughout the night. Nevertheless, there is in addition small-scale structure on top of the leading bore phase, wave-like structures that appear to have separations on the order of 0.5–2 km. For example, small-amplitude features are apparent in the frame 40 (middle row) all-mode panel plot while there is a suggestion of enhanced amplitudes in the frame 68 (bottom row) panel. The results shown in the left-hand column of Figure 4, which show the diff-mode line plots, present a better (although possibly distorted) picture of the fine structure. The distortion comes from the possible aliasing (or enhancement) of the fine structure when the differencing occurs. But the separations are consistent with the all-mode plots. In particular, the frame 68 panel only shows a portion of the pixel space to give a better idea of the fine structure. This plot suggests that the smallest structures could be separated by <500 m. These features are further discussed in Section 4.2.

3.2.4. The Relation of Vortex Rings to the Bore Phase Fronts

Figure 5 shows frame 92 of the all-mode movie taken at 235956 UT. Near the center bottom, there is a short black diagonal line that passes through an apparent vortex ring feature ahead of the leading edge of the leading bore phase. The separation of the peaks of the feature, which occur at pixel 138 and 161, is 23 pixels, or ∼1 km in diameter. A discussion of vortex rings and their origin can be found in Fritts et al. (2017) and Hecht et al. (2018) and references therein where they note that these features are associated with gravity wave breakdown.

3.3. Mean Temperature, Winds, and Other Derived Fields From the Na Lidar Data

In this section, we discuss the atmospheric structure employing the Na lidar data and the implications of these results for the properties of the bore and wave features discussed above. In these plots, the data are smoothed (and shown) every 6 min, and are additionally smoothed over 1.5 km in order to achieve relatively smooth profiles, and are displayed with 0.5-km resolution in Figures 6–8.

3.3.1. Mean Temperature and Winds

Figure 6 shows the zonal and meridional wind components and the temperature from 82 to 96 km during the period from turn-on, just before 000000 UT, to 040000 UT. There are several broad implications. In the region of interest from 82 to 88 km, at around 000000 UT, it is seen that there are no sharp temperature gradients but there are several regions of significant wind-shear. The zonal wind is westward up to ∼84/85 km, above which it reverses toward the east. The meridional wind is southward from about 83 to 86 km. Given that the apparent turbulence features advect slightly southward and westward, the wind components suggest that these features are located at ∼83–84 km. We also note that there is a strong negative temperature gradient above ∼87–88 km suggesting a region of evanescence that could form an upper boundary to a duct. Note that the winds at these higher altitudes are not in the direction of the advection of the small-scale features.

3.3.2. Atmospheric Stability and Evanescent Regions for Selected AGWs

Based on the data from Figure 6, the plots in Figure 7 show the resultant shear magnitude, N^2, and Ri values. The percentage error for both these values is about 30% in the 83–85-km altitude range. As above, the focus is on the period beginning at 000000 UT, where there is a region of enhanced shear below 84 km. The N^2 values are low above 88 km but high below 85 km. The resultant Ri values show values near (but mostly above 0.25) below 83 km. So, the background atmosphere may be close to instability in the that region.

Figure 8 presents the derived m^2 for two cases. The estimated error in m^2 for these results is about 30% based on the errors discussed above. Note, though that despite this uncertainty these results should be fairly accurate for estimating m^2 especially with respect to differentiating freely propagating regions from evanescent regions. The top panel shows the results for Equation 1 for a wave with a wavelength of 14.0 km that propagates toward the

Figure 2. ANI2 images at movie frame 16 at 234708 UT (top row), frame 40 at 235110 UT (middle row), and frame 68 at 235554 UT (bottom row). The two columns show images processed using the diff-mode (left) and all-mode (right) techniques. Both columns have images with a black solid diagonal line, at a fixed position in a direction that is approximately parallel to a bore phase crest. The right column images also have added white solid and black dashed diagonal lines that are approximately perpendicular to the bore phase crests. The white lines have pixel values of +10,000 while the black lines have pixel values of −10,000. The exposure time was about 3 s in all-mode and the difference time was 60 s. To orient, the viewer the zenith pixel and the approximate directions for north (0°), east (90°), south (180°), and west (270°) are marked.

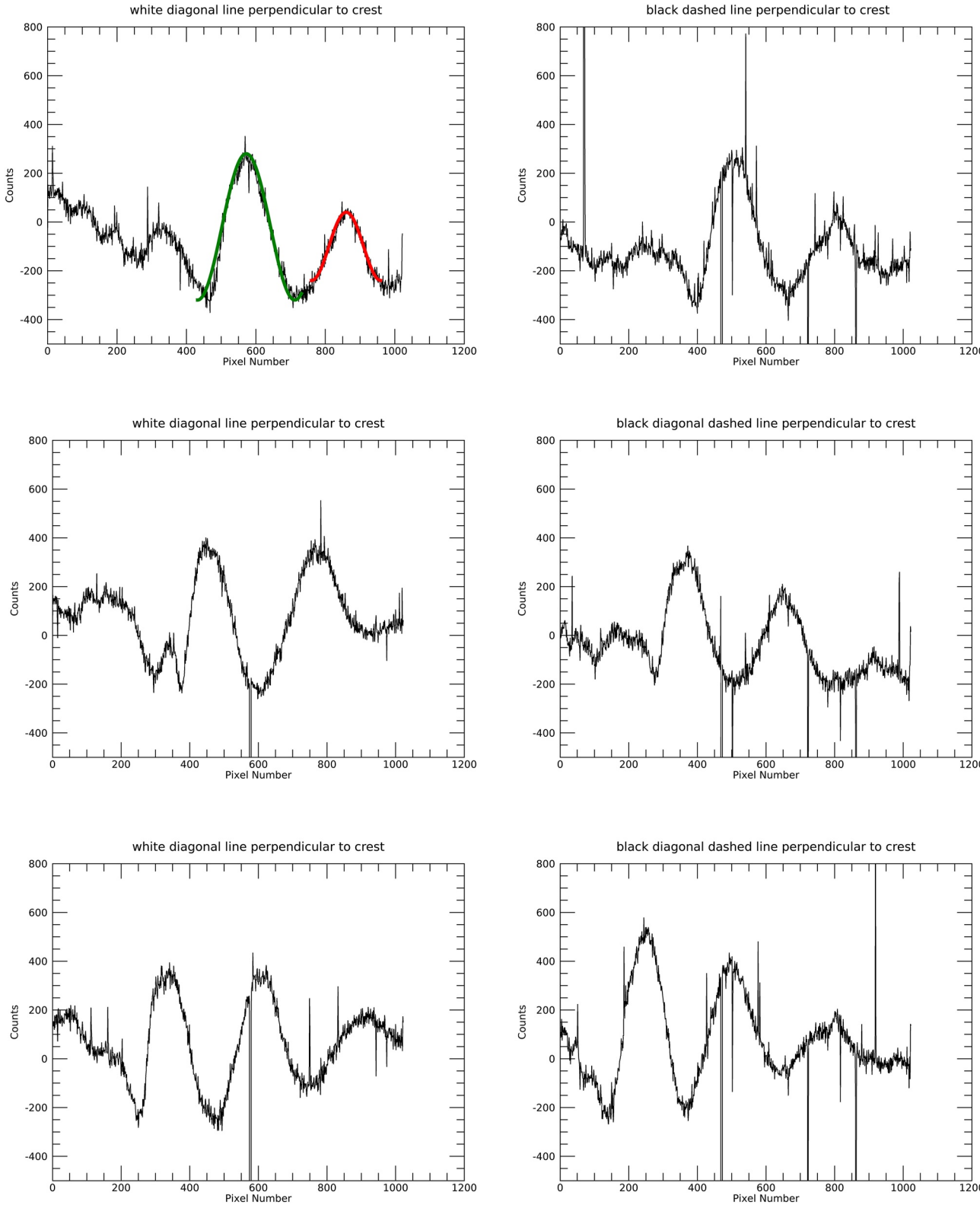

Figure 3. Plots of counts versus pixel number along the lines perpendicular to the phases associated with the all-mode images at right in Figure 2. Here, the left and right columns are for the white and black lines, respectively.

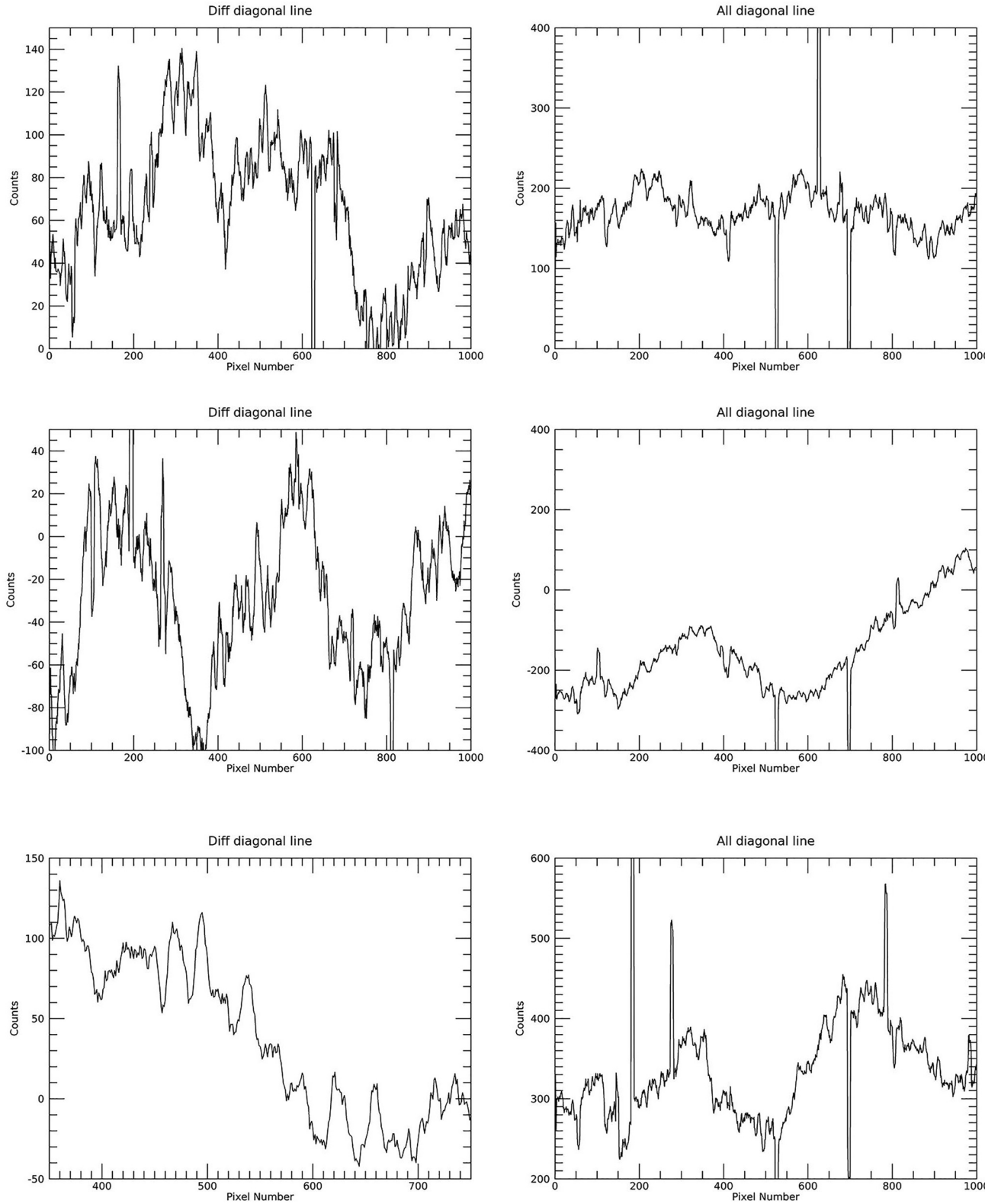

Figure 4. Plots of the counts versus pixel number of the diagonal lines parallel to the phases associated with the images of Figure 2. These plots correspond to the left and right columns of Figure 2. The lines are smoothed over 7 pixels.

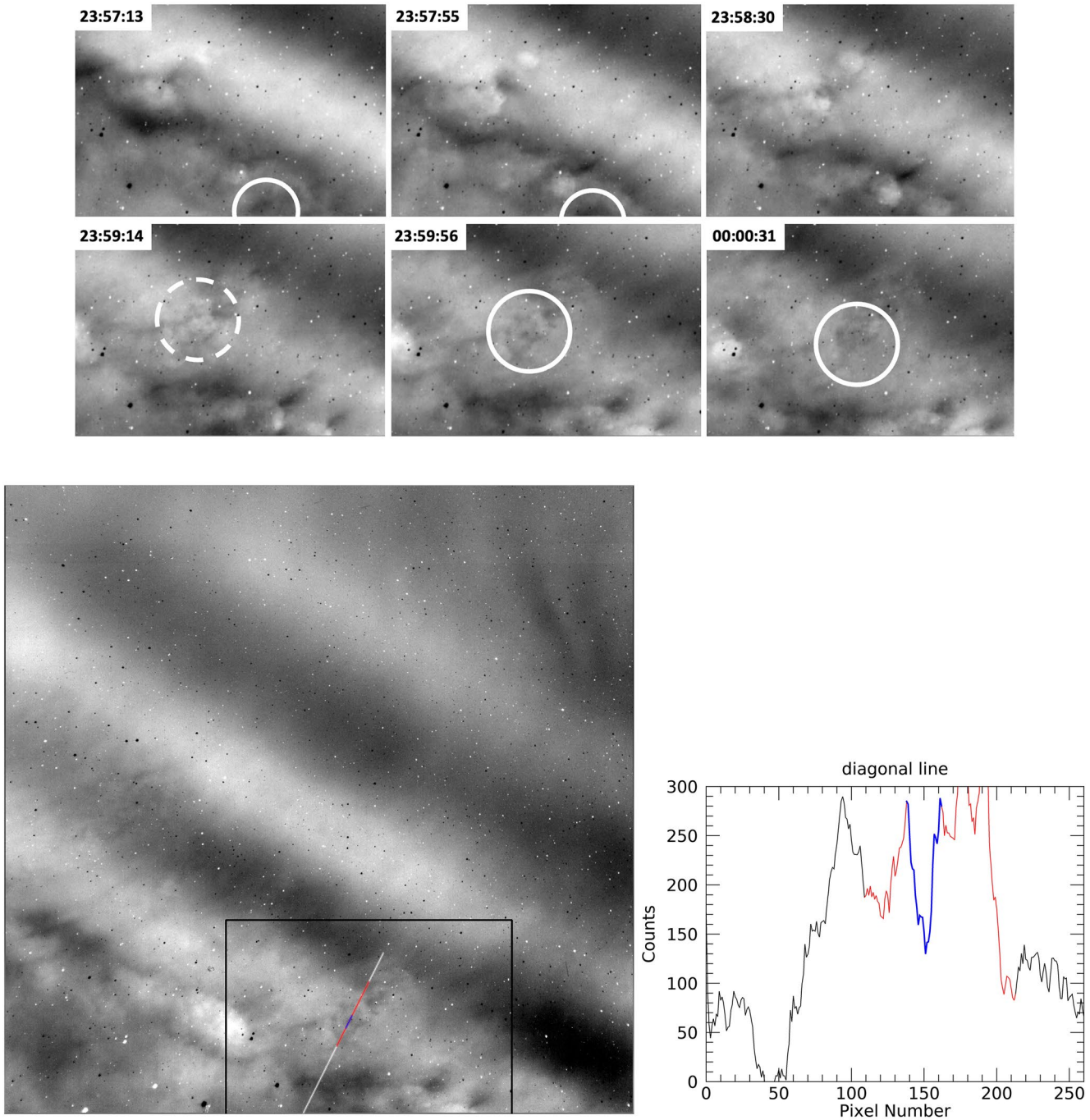

Figure 5. Illustrations of vortex ring morphology and development. At the top is a 6-panel (2-row) set of sections of images from the all-movie (Movie S3) with the times indicated in each frame. The white circles approximate the location of the vortex ring (with a diameter of ∼5 km). The top row shows a ring at the bottom of the image which is mostly off the image in the rightmost panel. The bottom row shows another sequence where the dashed circle shows its initial development. The vortex ring is best seen in the middle panel that corresponds to Frame 92 (at 235956 UT) of Movie S3. This entire frame is shown in the lower left image where the subsection shown above is outlined in black. The diagonal white line shows 261 pixels, where pixel 0 is at the bottom. Within that line there is a highlighted red portion that approximates a diameter of the white circle in the subsection. The over-plotted blue portion highlights a smaller donut shaped structure that has formed within the main vortex ring. A plot of the entire line, pixel 0 through pixel 260, is shown in the lower right panel where the blue and red highlights are as described.

SE at 149.4° at a velocity of 26.6 m/s. There is an altitude region between about 82.5 km on the bottom side and 87.5 km on the top side where such a bore or wave could freely propagate. Above and below the bore/wave would be evanescent and hence this defines a potential ducted region. Note, however, that the exact altitudes of the duct, especially at its lower boundary, are also uncertain because of uncertainties in the lidar data. We should also note

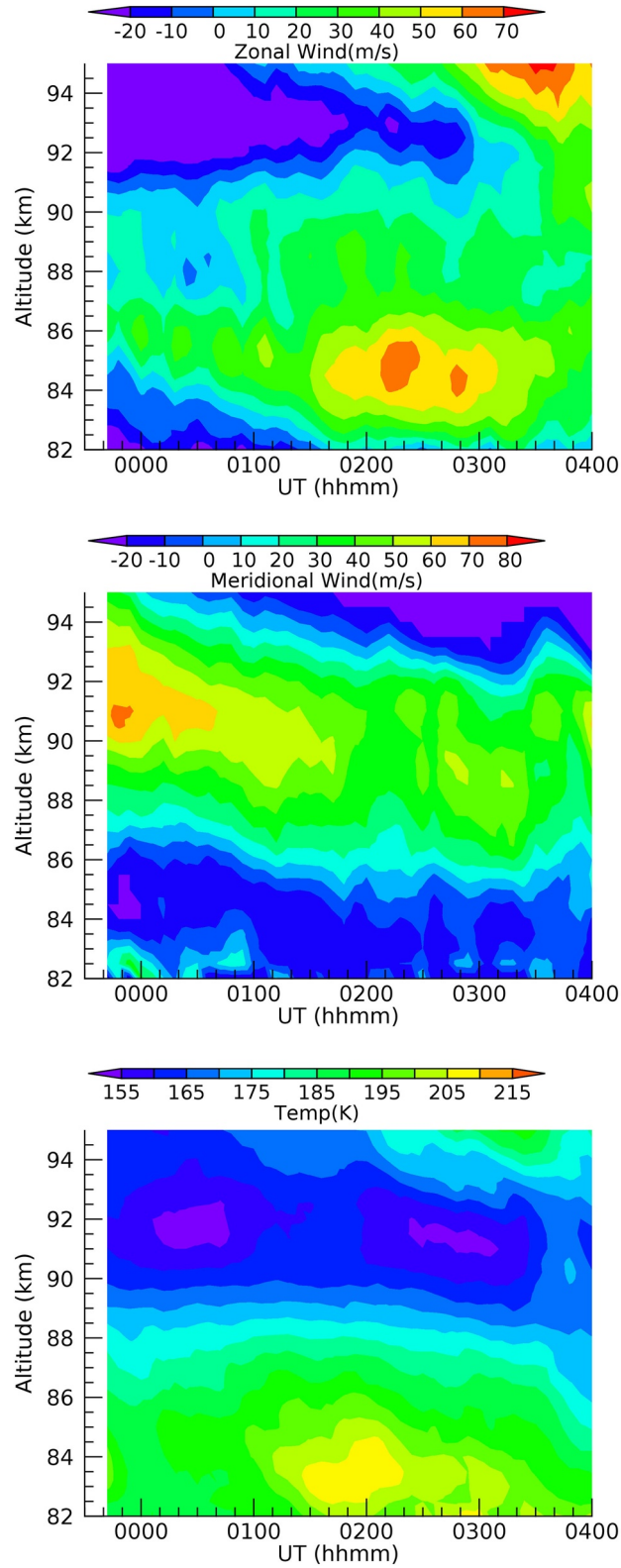

Figure 6. Three-panel plots of the derived measurements from the lidar data as functions of time and altitude where time is hhmm UT on 30 October 2016. Top is zonal (positive northward) wind. Middle is meridional (positive eastward) wind. Bottom is *T* at 5° intervals. For clarity, the colorbar only shows labels every 10°.

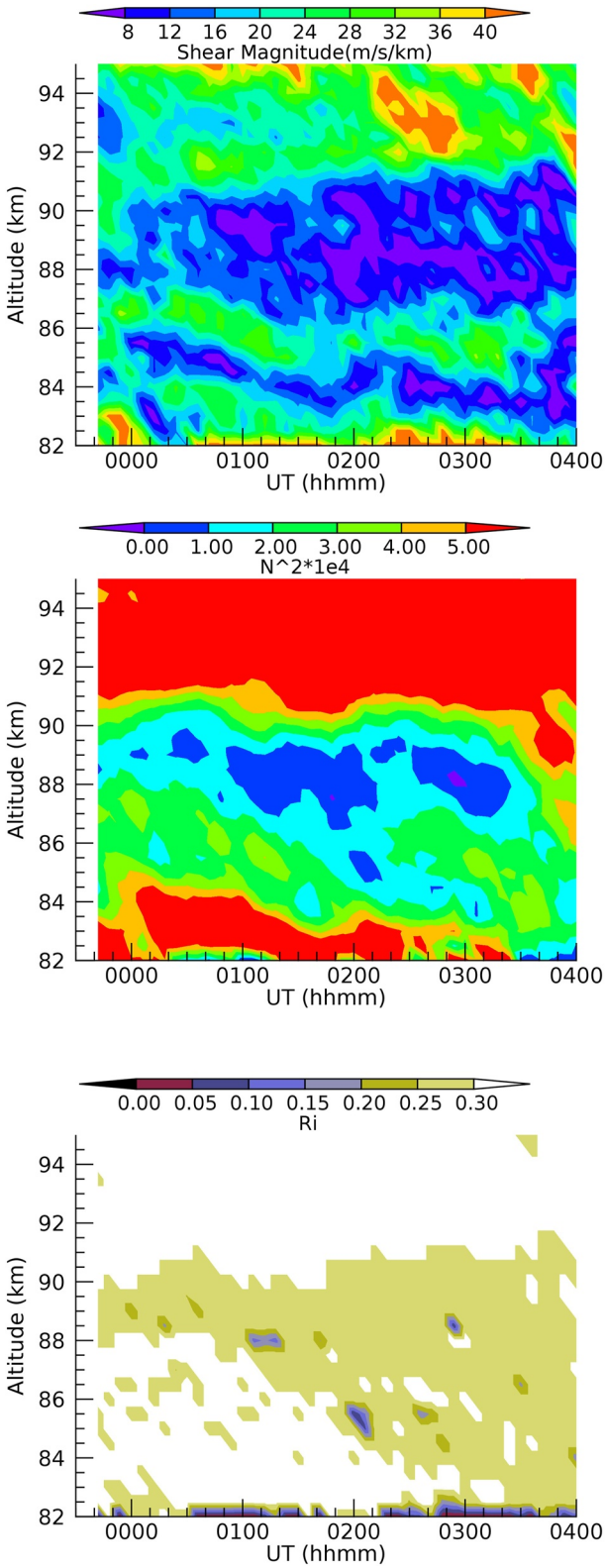

Figure 7. Three-panel plots of the derived measurements from the lidar data as functions of time and altitude where time is hhmm UT on 30 October 2016. Top, wind-shear magnitude in m/s/km. Middle, N^2 in units of $1/s^2$. Bottom, Ri.

though that the wind velocities used here are from the lidar data and hence may include some of the wind induced by the bore. However, based on data shown later that should only effect the period between ±10 min from 0 UT hr.

The bottom right panel shows the results for a wave propagating at almost right angles to the bore. This approximates the waves seen in the movies for most of the night after about 003000 UT. Interestingly, the only evanescent region is at about 84–86 km just before 000000 UT. There is a possible evanescent region up to about 86 km up until 003300 UT, but after that almost all of the OH emission region (altitude below 95 km) would support freely propagating AGWs. This is consistent with what is seen in the movies.

3.3.3. Wind Interactions and the Bore

A positive m^2 does not mean that another phenomenon cannot be occurring, such as wave breakdown, that could be affecting the bore lifetime. This is investigated in Figures 9–13 where, analogous to AGW breakdown, bore breakdown seems a likely cause of the appearance of instabilities in the previous images. Equation 1 is used to characterize the bore vertical wavelength.

Figure 9 shows the meridional and zonal wind components as a function of time every 0.5 km from 82.5 to 86.0 km. These plots allow a determination of the altitudes of the instabilities as the earlier discussion of these features suggested that their meridional velocity was small and somewhat southward while their zonal velocity was larger and westward. The corresponding instability altitudes are found to be between 83 and 84 km.

Figure 10 shows a composite similar to Figure 9 but now for the wind in the direction of the bore propagation (perpendicular to the phase front) defined earlier as toward the SE at 149.4°. The red dashed line shows the bore velocity. There are several aspects of note in these plots. (a) When the lidar data are first obtained the wind is below the bore velocity at all altitudes and thus there is no critical layer absorption as expected. (b) There is a small approximate 20 min oscillation in the wind, more noticeable in the higher altitude line plot. This is most probably due to the lidar sampling every 6 min of the bore that has a measured a period between 8 and 9 min. Note that at 83.5 km there is little phase variation with time and thus at this altitude the bore perturbation of the wind at 6-min sample averages has little effect on the wind magnitude. (c) There is no critical layer absorption occurring even when the background wind magnitudes appear to be above the red dashed line. That is because the lidar wind data are the sum of the background wind, which is below the bore velocity, and the bore-induced wind perturbation. (d) There also appears to be a large vertical wind gradient below 84 km.

Figure 11 shows the results of using some of the winds from Figure 10 in Equation 1 in order to obtain an estimate of the bore's vertical wavelength. We selected two altitudes, at 83.5 and 84 km, since the wind showed little variation in time and hence probably represented the background wind without the bore wind perturbation. The plot shows the results from Equation 1. At 83.5 and 84 km, where the wave appears to have the smallest perturbation on the magnitude of the background wind, the results suggest a vertical wavelength of around 8–10 km before the bore dissipation began. Thus, it seems probable that the vertical wavelength is larger than the region of free propagation that seems to be 5 km or less.

The data in Figure 12 show four profiles of 12-min averaged temperature through and surrounding the duct region. The profiles are centered at 18-min intervals from 2348 to 0042 UT. The two latest profiles are nearly identical

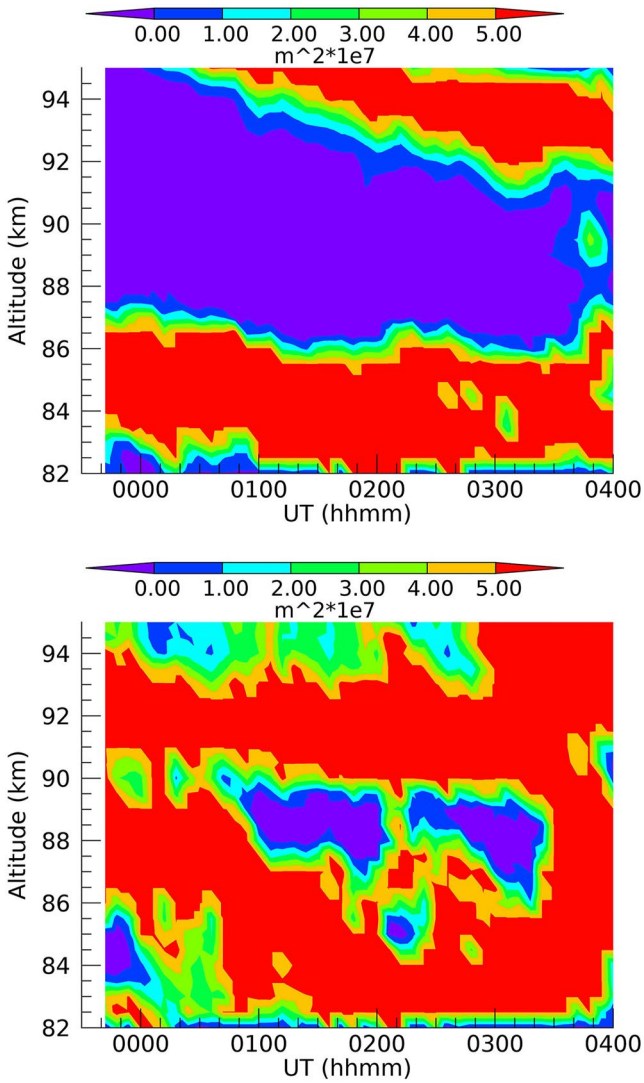

Figure 8. Two-panel plots of m^2 measurements, in units of $1/m^2$, from the lidar data as functions of time and altitude where time is hhmm UT on 30 October 2016. The values (multiplied by 1e7) are given in the colorbar. (top). A bore wave (14.0 km horizontal wavelength) propagating at 26.6 m/s and at an angle toward 149.4° where 180° is south (bottom of ANI2 image) and 90° is east (left side of ANI2 image). (top) Results using Equation 1. (bottom). Results for the same wave but traveling from SW toward the NE at about 45° and thus nearly perpendicular to the bore wave.

and most likely represent the prevailing undisturbed conditions. These profiles show a temperature maximum near 85-km altitude with a peak temperature of 194 K. The earliest profile (prebreakdown) shows warming (3 K) below the peak causing a downward displacement (1.5 km) of the temperature maximum. This is followed by a significant cooling (5–7 K) below 85 km that approximately restores the shape of profile during undisturbed conditions, but with an average offset of −4 K below 85 km. This scenario suggests first downward motion to lower the peak of the profile through primarily adiabatic compression and a rapid cooling due most likely to turbulent transport of heat away from the heated region. After the wave has dissipated, the temperature profile relaxes to its undisturbed conditions. Under this scenario, only the initial warming is caused by the direct action of the vertical winds associated with the bore.

Figure 13 shows one of the most interesting results of this study. The top panel shows the wind velocity in the bore direction from 82.5 to 90 km at two times, 234200 UT on 29 October before bore dissipation occurred and at 001800 UT on 30 October when the bore phases had dissipated, although residual turbulence remained. It should be noted that based on Figure 4 of Hecht et al. (2021) both the south and east observations taken at 234200 UT were taken before the leading bore phase arrived. For the observations at 001800 UT, the bore phases are aligned so that the maximum phase dissipation was occurring at or close to the south and east lidar positions. The bottom panel shows the difference between these two plots. Above 87 km, the difference is essentially zero but from 83.5 to 86 km, the difference is 10 ± 5 m/s. Interestingly the data suggest that below 83.5 km the difference increases and we note that this is part of the altitude regime where the turbulent-like features form. However, taken together these results are consistent with the bore dissipation accelerating the mean wind.

4. Discussion

The results of the observations presented above provide some answers and insights into the following questions.

4.1. Are the Observed Features Instabilities, AGWs, or Mesospheric Bore?

In an earlier review of airglow observations of waves and instabilities, Hecht (2004) concluded based on earlier studies that AGWs would typically have horizontal wavelengths above 15 km, while instability features would generally have wavelengths below 15 km. Furthermore, instabilities are blown with the mean wind while AGWs typically are not observed in the wind direction because they would likely dissipate upon encountering a critical level (e.g., Hecht et al., 2018) where the wave velocity equals the wind velocity in the direction of the wave. For the current observations, the horizontal wavelength is about 15 km and there is an altitude around 86 km where the wind velocity almost matches the wave velocity. However, there are several reasons why the data do not support the identification of the wave-like feature as an instability but rather as an AGW and/or mesospheric bore. First, there is only a narrow altitude regime, around 86 km, where the wave and wind velocity are close. Second, the motion of the turbulent features, which are clearly associated with the wave breakdown, indicates that they are located around 83 km where the wave and wind velocity are quite different. Third, some of the features seen during breakdown appear to be vortex rings, features associated with AGW breakdown, but not with the formation of a KHI (Hecht et al., 2018).

If these features are not instabilities, are they consistent with AGWs or mesospheric bores? To determine that one needs to have a definition of a mesospheric bore. Following DP98 and DP01 internal atmospheric bores

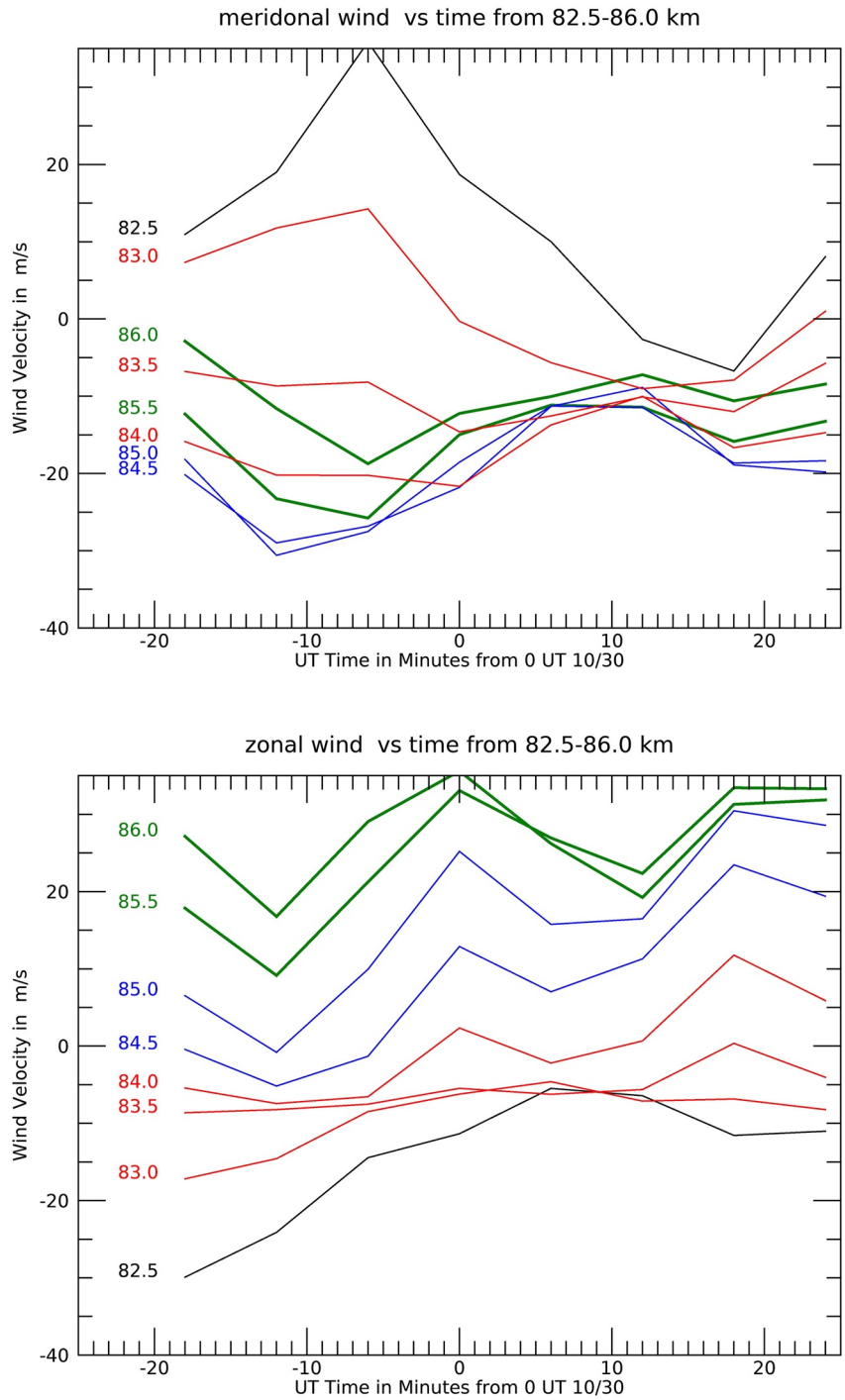

Figure 9. Plots of the wind speed in the zonal (bottom panel, positive north) and meridional (top panel, positive east) directions as a function of time and altitude.

are generally regarded as a class of nonlinear ducted-AGWs that are analogous to bores seen in river channels (Lighthill, 1978). Continuing the analogy, the leading wave phase is not symmetric but can develop, due to nonlinear effects, a steeper leading edge than a pure sinusoidal wave as discussed in Lighthill (1978). Waves with a steep leading edge that are considered mesospheric bores are both a feature of modeling (Laughman et al., 2009, 2011; Seyler, 2005) and of previous observations (e.g., Taylor et al., 1995; Walterscheid et al., 2012). The observations presented in this study therefore reveal (a) the presence of a duct, (b) a wave-like feature with a

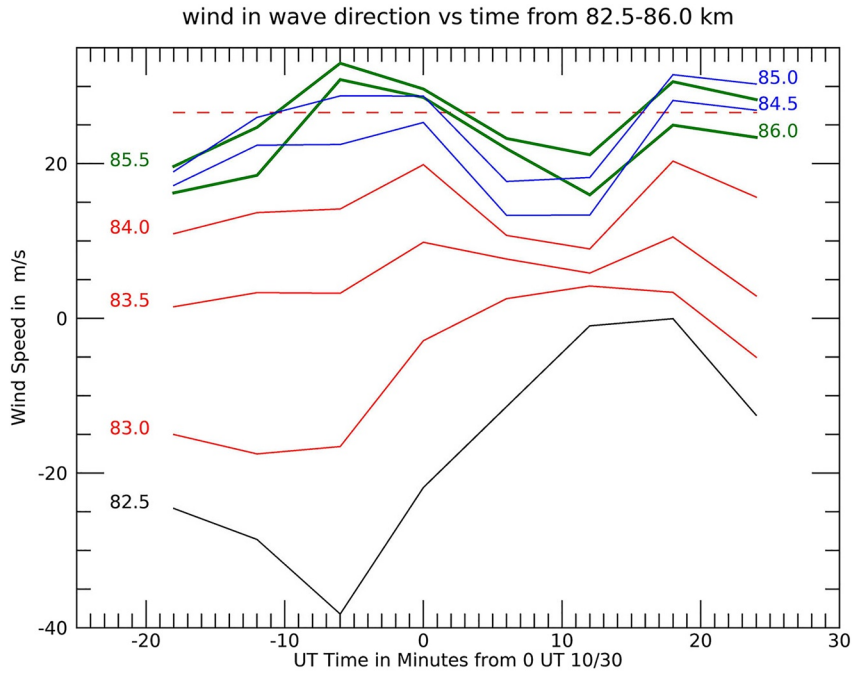

Figure 10. Plots versus time of the wind speed in the direction of the bore propagation direction toward the SE at 149.4°. The line plots are every 0.5 km in altitude from 82.5 to 86 km. A positive value is in the wave direction. The red dashed line is the bore phase velocity of 26.6 m/s.

vertical wavelength that would, as noted below, be consistent with being ducted, (c) a leading wave phase with a steep leading edge, and a limited number of observed phase fronts behind the leading edge. Hence, the identification of the waves seen in this study as a bore is consistent with these previous studies.

Even though these observations are for the dissipation and not the formation of the bore, for completeness, we also compare the observed characteristics of the bore (velocity, wavelength, amplitude) with several models.

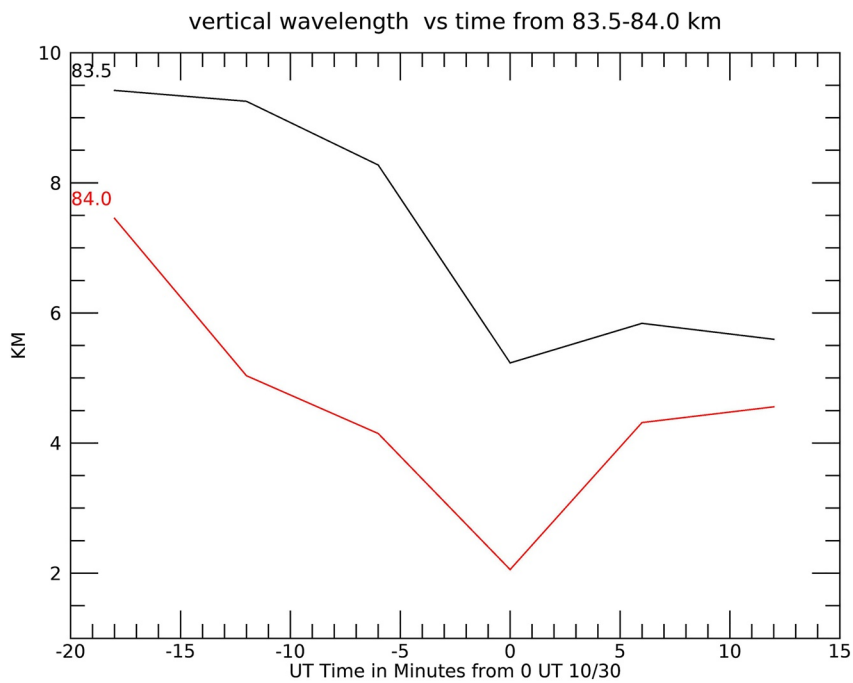

Figure 11. Plots of the bore vertical wavelength derived from the winds in Figure 10 and Equation 1.

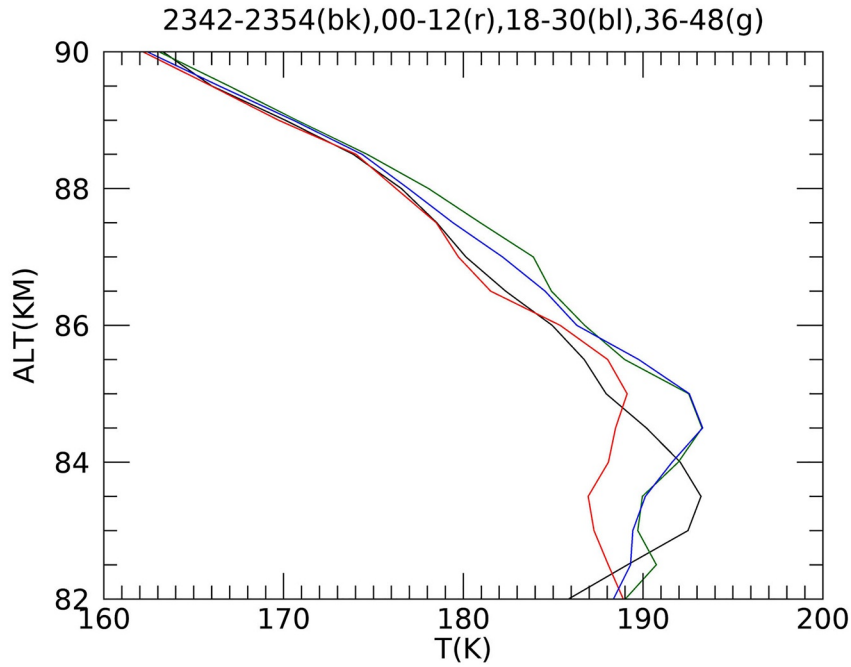

Figure 12. Line plots of the average over 12 min of the temperature profile from the lidar data. Black-2342–2354 UT on 29 October 2016. Red-0000–0012 UT on 30 October 2016. Blue-0018–0030 UT on 30 October 2016. Green-0036–0048 UT on 30 October 2016.

These include predictions from DP98 using the approach of Smith et al. (2003), hereafter SM03, and the more comprehensive modeling discussed in Seyler (2005). We note that neither of these models strictly cover the scenario described below where the observed wave is carried in a duct whose vertical wavelength is half the waves vertical wavelength. Since, however, in our case, the plane of symmetry is at the top of our duct we can use DP98 relations (Equations 2–4 in SM03) by noting that what they refer to as half-widths are full-width in our terminology. Hence, we approximate value the width of the duct after the bore jump, h_1 to be 4 km. An estimate of the increase due to the bore jump (see Figure 7 of DP98 and Figure 1 of SM03) is obtained following SM03 where we note that a temperature perturbation of about 5% (see the discussion below following our Equation 4) or about 10 K is equivalent to an amplitude of about 1 km. From Equation 4 of SM03, we can then solve for h_0, the duct width before the jump and find that value to be 2.8 km or a bore jump of 1.2 km. Interestingly, in Figures 7 and 12 of this paper, there appears to be an increase in the altitude of N^2 and an increase in the peak of T of just over 1 km (in the 83–85 km region) as the bore dissipates. Thus, a nominal jump of that magnitude seems reasonable and we take h_0 to be 2.8 km. The bore velocity can be calculated from Equation 7 (2) of DP98 or SM03, when assuming a value for the reduced gravitational acceleration, g'. Following DP98, we use a value of 1 for g' by calculating its value for altitudes of 85 and 86 km. The intrinsic bore velocity with respect to a fluid at rest is then around 70 m/s, a value above the observed bore velocity, although the wind velocity at the time of bore formation is not known and hence its intrinsic velocity is uncertain. The bore wavelength calculated from Equation 3 of SM03 would be predicted to be about 20 km, a little above the 14 km wavelength measured here. Using these values and following DP98, we note that the rate of bore formation from DP98 is a few per hour suggesting that, as only three phases are observed, the bore formation was recent.

Seyler (2005) had a somewhat more sophisticated modeling approach and those results are presented in their Table 1 and discussed in their paragraph 37. For this comparison, the layer thickness, h, is taken as 4 km and the reduced time scale ($1/N$) to be around 50 s using an N^2 value of 3e−4. However, we note Seylor did not run a case, appropriate to our observation, where the bore vertical wavelength was twice h. For Case 3, where the bore vertical wavelength equals h their reduced velocity is 0.6 resulting in a predicted velocity of $0.6 \times 4{,}000/50$ or 48 m/s. Nevertheless, with the observed wind velocity, at the beginning of these observations, being against the bore velocity, the intrinsic bore velocity could easily be close to the model prediction. Nevertheless, a more comprehensive model is needed for a clear numerical prediction of these observed bore parameters.

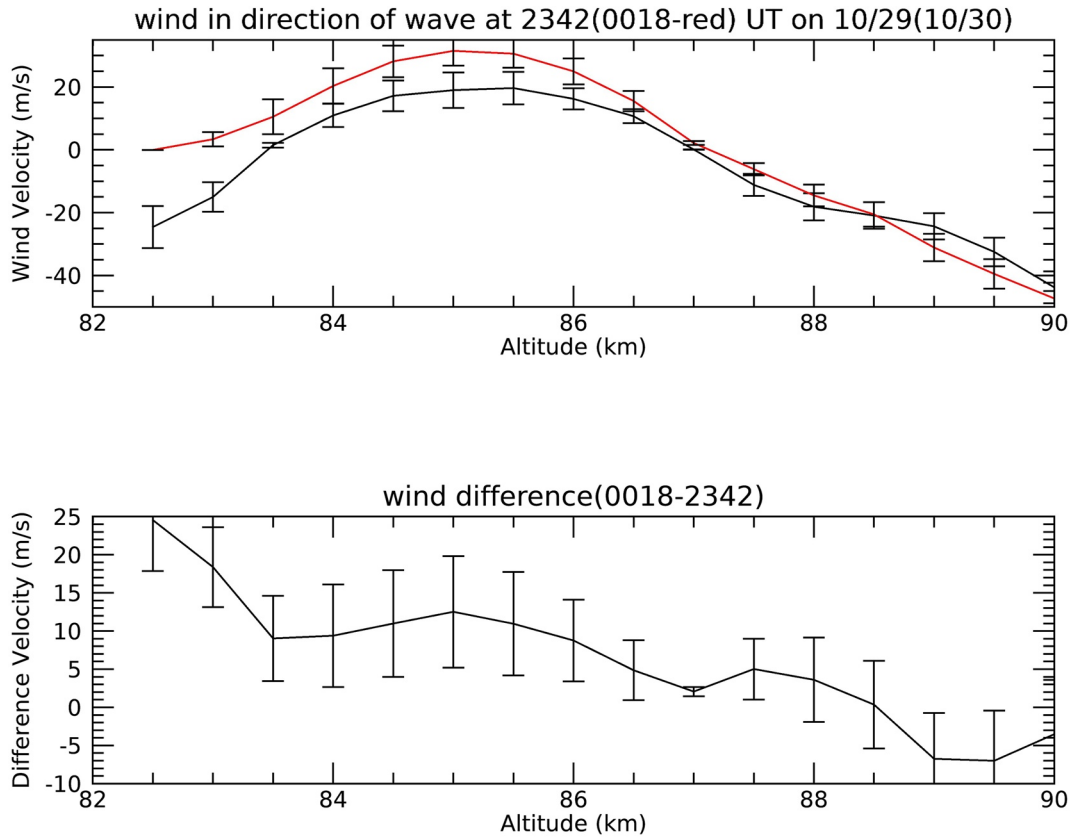

Figure 13. (top) Plot of the wind speed versus altitude for two different times toward the 149.4° direction. A positive value is in that direction. The two times are at 234200 UT on 29 October in black and 001800 UT on 30 October in red. (bottom) The difference in the wind speeds between 234200 and 001800 UT.

4.2. Breakdown of the Bore

In the observations discussed in this work thin features form perpendicular to the bore phase, followed by dissipation of the bore. Such features in previous work indicated the presence of convective overturning leading to a convective instability (Fritts et al., 1997; Hecht et al., 1997). We note that even in KHIs the secondary features that appear perpendicular to the main KHI phase are considered to be convective instabilities (e.g., Hecht et al., 2005). Thus, it might be expected that a bore would form an overturned convectively unstable region given that (a) the front of the leading wave phase is steep, with respect to its amplitude change with time, (b) the leading wave phase has the largest amplitude, and (c) the connection between OH airglow intensity and temperature (e.g., Snively et al., 2010; Walterscheid et al., 1987). While many of the bore observations cited in Section 1 do not show wave breakdown several of the recent studies do show ripple features that may be aligned somewhat perpendicular to the bore wave (Medeiros et al., 2018; Mondal et al., 2021). Hence, a decay of a bore via a convective overturning may be common. However, as a bore is essentially a trapped nonlinearly steepened AGW, and the observation of vortex ring structures as a byproduct of the breakdown suggests a complex route to turbulence, more sophisticated modeling is needed to determine the exact pathway to bore breakdown.

4.3. Momentum Flux Divergence in the Duct and the Acceleration of the Mean Wind

Solitary waves are finite amplitude ducted gravity wave trains distinguished by amplitude ordering. Bores are essentially solitary waves often with a turbulent leading edge. Figures 2 and 3 show a wave train and we assume that the observed wave train is generated elsewhere and propagates into the FOV. We base this interpretation on the fact that the phase lines (Figure 2) show no indication of curvature, strongly suggesting that the wave train is in the far field.

Waves can force the mean flow when one or more of the nonacceleration conditions are violated (Andrews & McIntyre, 1976; Eliasson & Palm, 1961). Nonacceleration does not mean momentum fluxes (or more generally

an Eliassen-Palm flux) are zero, rather that they are divergence free. The nonacceleration conditions that are potentially relevant in the present case include wave dissipation, nonlinearity, and transience. Although solitary waves are nonlinear and there are some modest amplitude variations these effects should be minor compared to the effect of the rapid dissipation of each phase following breakdown. Thus, for the present event, we address the effects of dissipation by means of wave breakdown. We examine whether the mean wind acceleration inferred from the divergence of this flux is large enough to allow a reasonable inference that the observed mean wind acceleration was caused by wave breakdown.

We examine mean wind acceleration induced by modal waves traveling horizontally in a preexisting duct. Following Grimshaw (1984), we address the vertically averaged acceleration within the duct. In the far field away from external forcing at the duct boundaries, vertical averaging gives conservation equations in terms of which only contributions from horizontal fluxes survive, and the only relevant dependencies are on the horizontal coordinates (Andrews & Mcintyre, 1978b; Grimshaw, 1984). Vertical averaging reduces the divergence of the flux of horizontal momentum to the term involving only the horizontal wind perturbation. We emphasize that in the far field where modal structure prevails and where the duct is not subject to external forcing the vertical flux of momentum plays no role in the mean wind acceleration averaged over the duct.

Wave forcing of the mean flow is given by

$$\partial \overline{\mathrm{u}}(x,t)/\partial \mathrm{t} + \mathrm{U}\partial \overline{\mathrm{u}}(x,t)/\partial \mathrm{x} = -\partial \mathrm{M}(x,t)/\partial \mathrm{x} \tag{2a}$$

where $M = \overline{\mathrm{u}'^2}$ and where primes denote perturbation quantities and overbars denote density weighted averages over the duct cross-section and ensemble averages over phase in the moving frame (Andrews & Mcintyre, 1978a, 1978b; Bühler, 2014; Grimshaw, 1984). The overbar commutes with the x and t derivatives. We include the advective effects of the background time-independent part of the vertically averaged mean wind (denoted U). In writing Equation 2a, we have used the fact implicit in the definition of $\overline{\mathrm{u}}$ that the local time tendency is dominated by variations in $\overline{\mathrm{u}}$ transported with the waveform. Thus, Equation 2a can be written as

$$(\mathrm{U} - \mathrm{c})\partial \delta\overline{\mathrm{u}}/\partial \mathrm{x} = -\partial \mathrm{M}/\partial \mathrm{x} \tag{2b}$$

where $\delta\overline{\mathrm{u}}$ is the wave-induced change in $\overline{\mathrm{u}}$. It is assumed that M at the leading edge of the waveform is essentially zero after initial breakdown and has its maximum value, M_0 at the trailing edge until just before breakdown occurs there. Similar remarks apply to $\delta\overline{\mathrm{u}}$. Integrating Equation 2a over the waveform just before breakdown occurs at the trailing edge gives

$$\delta\overline{\mathrm{u}} = \frac{1}{\mathrm{c} - \mathrm{U}} M_0 \tag{3}$$

Equation 3 is an upper limit wherein it is also assumed that the wave remains ducted.

We note that the result given in Equation 2b can be obtained by a simple heuristic argument wherein $\delta\overline{\mathrm{u}} = \tau(M_0/\mathrm{L})$, where τ is the time elapsed from initial breakdown at the leading edge x_b of the waveform to the time the trailing edge passes, and L is the x-dimension of the volume of fluid affected in time τ in the intrinsic frame, whence $L = (c - U)\tau$. The quantity M_0/L is the mean flux divergence over the volume of fluid affected and τ is the time it acts. Thus, at x_b, $\delta\overline{\mathrm{u}} = M_0/(c - U)$.

The vertical and phase averages are both average over waveforms. Each average contributes a factor of about 1/2 reduction with respect to the amplitude of the wave. This is an estimate because neither waveform is precisely sinusoidal. Thus,

$$M = \frac{1}{4}|\mathrm{u}'_{\max}|^2 \tag{4}$$

As noted above Figures 2 and 3 show a wave train with three amplitude-ordered waves, each wave comprising a light and dark phase. The bore phases are progressively less steep ordered from the leading to the trailing phase. We note that for the observed wave train each individual wave, breaks down independently and breakdown occurs in approximately the same place. Since momentum flux is a quadratic quantity and the summed squares of the amplitudes of the two trailing waves is a significant fraction of the squared amplitude of the leading one, we expect the trailing waves to contribute to the observed acceleration. We note that by reducing the intrinsic phase

velocity the breakdown of a wave conditions the atmosphere so that the following phases should breakdown at smaller amplitude, perhaps explaining why the individual phases break down in roughly the same location (Orlanski & Bryan, 1969). Hence, to estimate M, a value for u'_{max} (the amplitude of the wave) needs to be determined. For the current observations, the bore is presumably ducted and any phase cancelation that might affect the LOS integrated intensity (Swenson et al., 1998) depends on the dominant ducted mode. Here, we argue that the most likely mode by far is the fundamental where the vertical structure has the approximate form of a half wave cycle, so that the intensity of a phase in the duct seen at a fixed location alternates between entirely positive and entirely negative as the waveform passes (Walterscheid & Hickey, 2009). The next higher mode with, say, positive over negative in one phase of the wave and negative over positive in the other, would give greatly reduced contrast across the waveform in the vertically integrated intensity and the waveform would be much less distinct. Yet higher modes would give implausibly short vertical wavelengths that are distinctly inconsistent with the dispersion relation. The dispersion relation favors vertical wavelengths ~8 km, which is consistent with a half-cycle contained in a 4 km thick duct.

In Appendix A, it shown that for the fundamental the relationship between the inferred temperature perturbation and the measure airglow intensity perturbation is given by

$$\frac{\hat{T}}{T_B} \sim 0.8 \frac{\langle I' \rangle}{\langle \bar{I} \rangle} \tag{5}$$

where here the subscript B refers to the background temperature without the bore structure and the $\hat{T}$ represents the amplitude of the bore temperature perturbation. Thus, the left-hand side represents the amplitude of the fractional temperature fluctuation within the bore. The right-hand side represents the measured fractional intensity fluctuation where the $\bar{I}$ is the mean background intensity whose corresponding fluctuation is I'. Here, the angle brackets denote that the quantities are vertically integrated. We note that the 0.8 factor depends on Krassovsky's ratio as discussed in Appendix A. For these data, the measured fractional intensity is 0.06 and hence the inferred fractional temperature perturbation is taken as 0.06×0.8 or 0.048.

An estimate of the wind perturbation is obtained from the relation between the wind perturbation and the fractional temperature perturbation that is discussed in Hecht et al. (1997) and Walterscheid and Schubert (1990). This relation is

$$u'_{max} = \frac{\hat{T}}{T_B} \frac{g}{N} \tag{6}$$

where here N is taken as about 0.022 s^{-1}, and g is 9.5 ms^{-2}. The value of N has an uncertainty on the order of 10%. Using Equation 6, the value for u'_{max} is ~20.7 m/s for the leading wave. The two trailing waves would have u'_{max} values of ~15 and 5 m/s, respectively, based on their peak amplitudes relative to the leading wave.

To calculate $\delta\bar{u}$ from Equation 3, values for M, c, and $\bar{u}$ are needed. Using the estimate of u'_{max} as ~20.7 m/s, the momentum flux associated with the leading wave in the bore is about 0.25×20.7^2 or ~105 m^2/s^2. The value for $\bar{u}$ is taken to be the mean wind in the duct from the winds plotted in Figure 10 at the beginning of the lidar observations. This value of 6 m/s is also close to the value for the winds at 83.5 and 84 km, the altitude region least affected by the passage of the bore. The bore velocity, c, is taken as 29 m/s as discussed earlier. Thus, $\delta\bar{u}$ is ~105/(29 − 6) or about 4–5 m/s due to the dissipation of the first bore wave. Based on the values for u'_{max} cited above for the two trailing waves, there could be an additional 3 m/s wind acceleration if they dissipate at the same location as the imaging suggests. Thus, the total estimate of $\delta\bar{u}$ is ~7–8 m/s.

We note that we cannot estimate a lower limit to u'_{max} from the lidar data because these data are reported on 6-min intervals while the wave period is just over 8 min. Thus, the wave period is less than the aliasing period.

The data in Figure 13 suggest the measured value for $\delta\bar{u}$ is about 10 ± 5 m/s in the duct between 83 and 86 km, and significantly larger below 83.5 km. This is obtained by considering the difference in the wind at the time the lidar observations began on 29 October that was before any dissipation occurred and at a later time (18 min UT on 30 October) when the bore waves have mostly dissipated. We conclude that the theoretically derived $\delta\bar{u}$ is large enough to allow a reasonable inference that the observed acceleration is induced by the bore, despite the uncertainties in the approach. The greatest uncertainty is the additive nature of the second and third waves which must be considered, as we have applied it, an upper limit.

One interesting aspect of the observations shown in the bottom panel of Figure 13 is that, as mentioned, there seems to be a larger increase in the wind acceleration toward the bottom of the duct where the breakdown seems to have been initiated. The estimation approach presented here assumes that quantities are characteristic of values within the duct interior and does not account for this detail and more complete dynamical modeling is needed to understand that observation.

5. Summary

This study presents the first comprehensive high-spatial resolution observations of the dissipation of a mesospheric bore. A series of wave phases were observed and their morphology suggested that they were the manifestations of a mesospheric bore. Three aspects strongly suggested this identification was appropriate, rather than that of an AGW or an instability. First, was the presence of a steep leading edge of the leading wave phase that is therefore manifested as a nonsinusoidal wave form, often a hallmark of mesospheric bore observations and modeling. Second, was the fact that when bore breakdown occurred, the resultant instabilities were blown by the wind in a direction consistent with an altitude well-removed from the altitude where the bore phase velocities and wind directions were close to (but not) coincident. Third, some vortex ring instability features were seen that are characteristic of the breakdown of an AGW rather than of an instability. We suggest that the bore probably broke down due to the development of a convective instability associated with the steep leading edge of the leading bore phase.

The wind observations showed that there was an acceleration of the mean wind of about 5–15 m/s The momentum flux associated with the bore was estimated to be ∼105 m^2/s^2 for the first bore wave leading to a wind acceleration of about 4–5 m/s. The trailing waves could together contribute about 3 m/s. Thus, the bore dissipation could account for the observed wind increases. Taken together this suggests that bore dissipation and break down could be a significant contributor to the dynamics of the mesopause region of the atmosphere.

Appendix A: Relation Between Airglow Temperature and Intensity Perturbations

The vertically integrated temperature fluctuation may be related to the vertically integrated intensity fluctuation by

$$\frac{\langle T'_I \rangle}{\langle \overline{T}_I \rangle} = \frac{1}{\langle \eta \rangle} \frac{\langle I' \rangle}{\langle \bar{I} \rangle} \tag{A1}$$

where angle brackets refer to vertical integration, the subscript I refers to emission weighted temperature and $\langle \eta \rangle$ is Krassovsky's ratio (Schubert et al., 1991). The goal is to relate local values of $\langle T'_I \rangle / \langle \overline{T}_I \rangle$ in the duct to the observed values of $\langle I' \rangle / \langle \bar{I} \rangle$.

The expression to be evaluated is

$$\frac{\left\langle T'_I \right\rangle}{\left\langle \overline{T}_I \right\rangle} = \frac{1}{\left\langle \bar{I} \right\rangle} \int \bar{I} \frac{T'}{\left\langle \overline{T}_I \right\rangle} \tag{A2}$$

The denominator of Equation A2 is

$$\langle \bar{I} \rangle \langle \overline{T}_I \rangle = \int \bar{I}\, \overline{T} dz$$

where

$$\overline{T} = \overline{T}_B(z) + \overline{T}_D(z)$$

and where the subscript B refers to the background without the duct structure and D refers to the duct structure. The position of the duct within the emission layer, particularly as it affects the relative heights of the temperature and intensity maxima, affects the observed temperature perturbation relative to the intensity perturbation (Swenson & Gardner, 1998). In the following analysis, we make the simplifying and conservative assumption that the duct and emission layer are centered at the same altitude which we take to $z = 0$. Our assumption

is conservative in the sense that it yields a smaller value of $T_I'/\overline{T}_I$ based on observations of $\langle I' \rangle / \langle \bar{I} \rangle$. The assumption maximizes the intensity weighting and thus maximizes the multiplier of $T_I'/\overline{T}_I$on the left side of Equation A2.

We assume that the duct and emission layers have Gaussian profiles with e-folding half-widths of δ_D and δ_I, respectively. If $\overline{T}_B$ does not vary too rapidly over the emission layer and $\delta_D = \alpha\delta_I$ then approximately

$$\langle \bar{I} \rangle \langle \overline{T}_I \rangle = \sqrt{\pi}\delta_I \bar{I}(0)\overline{T}_B + \sqrt{\pi}\delta_{DI}\bar{I}(0)\overline{T}_D(0)$$

$$\delta_{DI}^2 = \frac{\alpha^2}{(1+\alpha^2)}\delta_I^2$$

where δ_{DI} is the half-width of the product of the two Gaussian and $\overline{T}_B$ is redefined as the average value in the neighborhood of $z = 0$. The duct is about 4-km thick and a nominal thickness for the emission layer is 8 km, giving $\alpha = 1/2$ and $\delta_{DI} = \delta_I/\sqrt{(5)}$ with the result

$$\langle \bar{I} \rangle \langle \overline{T}_I \rangle = \sqrt{\pi}\delta_I \bar{I}(0)\overline{T}_B + \left(1/\sqrt{(5)}\delta_I\, \bar{I}(0)\overline{T}_D(0)\right.$$

For a duct with a 4-km width, the second term may be neglected because the temperature excursion $\overline{T}_D(0)$ can be no greater than ~20 K. This gives

$$\frac{\langle T_I' \rangle}{\langle \overline{T}_I \rangle} = \frac{1}{\sqrt{(\pi)}\delta_I \bar{I}_0}\int_{-\delta/2}^{\delta/2} \frac{\bar{I}T'}{\overline{T}_B}\mathrm{dz}$$

where the limits of the integral reflect the restriction of temperature fluctuations to the duct. We take the variation of T' over the duct to reflect the fundamental so that $T' = \hat{T}\cos(\pi/\delta_D)z$. Since the variation of $\bar{I}$ over the duct is slower than the variation of T' approximately

$$\int_{-\delta/2}^{\delta/2} T'\mathrm{dz} = \frac{2\delta_D}{\pi}\hat{T}$$

and

$$\frac{\langle T_I' \rangle}{\langle \overline{T}_I \rangle} = \frac{2\delta_D}{\pi^{3/2}\delta_I}\frac{\hat{T}}{T_B} = \pi^{-3/2}\frac{\hat{T}}{T_B} \tag{A3}$$

A more accurate and tedious integration accounting for the variation of $\bar{I}$ over the duct gave a slightly smaller (less conservative) multiplier. Using Equation A3 in Equation A1 gives

$$\frac{\hat{T}}{T_B} = \frac{\pi^{3/2}}{\langle \eta \rangle}\frac{\langle I' \rangle}{\langle \bar{I} \rangle} \tag{A4}$$

For the present case, where the emission and temperature fluctuation are limited to the duct and phase cancelation does not occur, the single level value from Walterscheid et al. (1987) seems appropriate. This gives $\eta \sim 7$, considering the measured period of <600 s and a small background wind with respect to the measured phase velocity. Thus,

$$\frac{\hat{T}}{T_B} \sim 0.8\frac{\langle I' \rangle}{\langle \bar{I} \rangle}$$

We note that for waves in the dynamics only regime, where wave frequency is much greater than the inverse of chemical time scales (such as for the present waves), the value of Krassovsky's ratio for a finite emission layer is similar to the single layer value, indicating much less sensitivity for Krassovsky's ratio to cancelation effects than for $\langle T_I' \rangle / \langle \overline{T}_I \rangle$ and $\langle I' \rangle / \langle \bar{I} \rangle$ individually (Schubert et al., 1991; Walterscheid et al., 1987).

Data Availability Statement

The lidar data (Liu et al., 2016) are available at zenodo.org. The imager data needed for this paper in Figures 2–5 (Hecht et al., 2023) are also available at zenodo.org.

Acknowledgments
We thank Steve Heathcote and the staff at the Cerro Tololo Inter-American Observatory and especially at SOAR on Cerro Pachón for providing support for all the instrumentation and for the operations at the ALO. Support for JHH, LJG, RJR, and RLW was provided by NSF Grant AGS1450660 and AGS1911952. The UIUC/ERAU Na lidar operation at ALO was supported by NSF Grants AGS-1136278 and AGS-1136208. Support for DCF was provided by Grants NSF AGS-1445783 and AGS-1449633, AFOSR FA9550-18-1-0009, and NASA 80NSSC18K0007. The work by Alan Liu was supported while serving at the National Science Foundation. Any opinions, findings, and conclusions or recommendations expressed in this material are those of the authors and do not necessarily reflect the views of the National Science Foundation. The authors acknowledge Dr. Fabio Vargas for his work on imager operation at ALO.

References

Andrews, D. G., & McIntyre, M. E. (1976). Planetary waves in horizontal and vertical shear: The generalized Eliassen-Palm relation and the mean zonal acceleration. *Journal of the Atmospheric Sciences*, *33*(11), 2031–2048. https://doi.org/10.1175/1520-0469(1976)033⟨2031:PWIHAV⟩2.0.CO;2

Andrews, D. G., & Mcintyre, M. E. (1978a). An exact theory of nonlinear waves on a Lagrangian-mean flow. *Journal of Fluid Mechanics*, *89*(4), 609–646. https://doi.org/10.1017/S0022112078002773

Andrews, D. G., & Mcintyre, M. E. (1978b). On wave-action and its relatives. *Journal of Fluid Mechanics*, *89*(4), 647–664. https://doi.org/10.1017/S0022112078002785

Benjamin, T. B. (1967). Internal waves of permanent form in fluids of great depth. *Journal of Fluid Mechanics*, *29*(3), 559–592. https://doi.org/10.1017/S002211206700103X

Bühler, O. (2014). *Waves and mean flows, Chapter 2* (2nd ed.). Cambridge University Press. https://doi.org/10.1017/CBO9781107478701

Dewan, E. M., & Picard, R. H. (1998). Mesospheric bores. *Journal of Geophysical Research*, *103*(D6), 6295–6305. https://doi.org/10.1029/97JD02498

Dewan, E. M., & Picard, R. H. (2001). On the origin of mesospheric bores. *Journal of Geophysical Research*, *106*(D3), 2921–2927. https://doi.org/10.1029/2000JD900697

Einaudi, F., & Hines, C. (1970). WKB approximation in application to acoustic-gravity waves. *Canadian Journal of Physics*, *48*(12), 1458–1471. https://doi.org/10.1139/p70-185

Eliasson, A., & Palm, E. (1961). *On the transfer of energy in stationary mountain waves* (Vol. 22). Geofysiske publikationer.

Fritts, D. C., & Alexander, M. J. (2003). Gravity wave dynamics and effects in the middle atmosphere. *Reviews of Geophysics*, *41*(1), 1003. https://doi.org/10.1029/2001RG000106

Fritts, D. C., Isler, J. R., Hecht, J. H., Walterscheid, R. L., & Andreassen, Ø. (1997). Wave breaking signatures in sodium densities and OH nightglow: 2. Simulation of wave and instability structures. *Journal of Geophysical Research*, *102*(D6), 6669–6684. https://doi.org/10.1029/96JD01902

Fritts, D. C., Kaifler, N., Kaifler, B., Geach, C., Kjellstrand, C. B., Williams, B. P., et al. (2020). Mesospheric bore evolution and instability dynamics observed in PMC Turbo imaging and Rayleigh lidar profiling over Northeastern Canada on 13 July 2018. *Journal of Geophysical Research: Atmospheres*, *125*, e2019JD032037. https://doi.org/10.1029/2019JD032037

Fritts, D. C., Wan, K., Werne, J., Lund, T., & Hecht, J. H. (2014). Modeling the implications of Kelvin-Helmholtz instability dynamics for airglow observations. *Journal of Geophysical Research: Atmospheres*, *119*, 8858–8871. https://doi.org/10.1002/2014JD021737

Fritts, D. C., Wang, L., Baumgarten, G., Miller, A. D., Geller, M. A., Jones, G., et al. (2017). High-resolution observations and modeling of turbulence sources, structures, and intensities in the upper mesosphere. *Journal of Atmospheric and Solar-Terrestrial Physics*, *162*, 57–78. https://doi.org/10.1016/j.jastp.2016.11.006

Fritts, D. C., Wang, L., Geller, M. A., Lawrence, D. A., Werne, J., & Balsley, B. B. (2016). Numerical modeling of multiscale dynamics at a high Reynolds number: Instabilities, turbulence, and an assessment of Ozmidov and Thorpe scales. *Journal of the Atmospheric Sciences*, *73*(2), 555–578. https://doi.org/10.1175/JAS-D-14-0343.1

Fritts, D. C., Wang, L., Werne, J., Lund, T., & Wan, K. (2009a). Gravity wave instability dynamics at high Reynolds numbers. Part I: Wave field evolution at large amplitudes and high frequencies. *Journal of the Atmospheric Sciences*, *66*(5), 1126–1148. https://doi.org/10.1175/2008JAS2726.1

Fritts, D. C., Wang, L., Werne, J., Lund, T., & Wan, K. (2009b). Gravity wave instability dynamics at high Reynolds numbers. Part II: Turbulence evolution, structure, and anisotropy. *Journal of the Atmospheric Sciences*, *66*(5), 1149–1171. https://doi.org/10.1175/2008JAS2727.1

Fritts, D. C., Wieland, S. A., Lund, T. S., Thorpe, S. A., & Hecht, J. H. (2021). Kelvin-Helmholtz billow interactions and instabilities in the mesosphere over the Andes Lidar Observatory: 2. Modeling and interpretation. *Journal of Geophysical Research: Atmospheres*, *126*, e2020JD033412. https://doi.org/10.1029/2020JD033412

Grimshaw, R. (1984). Wave action and wave-mean flow interaction, with application to stratified shear flows. *Annual Review of Fluid Mechanics*, *16*(1), 11–44. https://doi.org/10.1146/annurev.fl.16.010184.000303

Hecht, J. H. (2004). Instability layers and airglow imaging. *Reviews of Geophysics*, *42*, RG1001. https://doi.org/10.1029/2003RG000131

Hecht, J. H., Fritts, D. C., Gelinas, L. J., Rudy, R. J., Walterscheid, R. L., & Liu, A. Z. (2021). Kelvin-Helmholtz billow interactions and instabilities in the mesosphere over the Andes Lidar Observatory: 1. Observations. *Journal of Geophysical Research: Atmospheres*, *126*, e2020JD033414. https://doi.org/10.1029/2020JD033414

Hecht, J. H., Fritts, D. C., Wang, L., Gelinas, L. J., Rudy, R. J., Walterscheid, R. L., et al. (2018). Observations of the breakdown of mountain waves over the Andes Lidar Observatory at Cerro Pachón on 8/9 July 2012. *Journal of Geophysical Research: Atmospheres*, *123*, 276–299. https://doi.org/10.1002/2017JD027303

Hecht, J. H., Liu, A. Z., Walterscheid, R. L., & Rudy, R. J. (2005). Maui mesosphere and lower thermosphere (Maui MALT) observations of the evolution of Kelvin-Helmholtz billows formed near 86 km altitude. *Journal of Geophysical Research*, *110*, D09S10. https://doi.org/10.1029/2003JD003908

Hecht, J. H., Ramsay Howat, S. K., Walterscheid, R. L., & Isler, J. R. (1995). Observations of variations in airglow emissions during ALOHA-93. *Geophysical Research Letters*, *22*(20), 2817–2820. https://doi.org/10.1029/95GL03019

Hecht, J. H., Rudy, R. J., & Gelinas, L. J. (2023). Data files for a "boreing" night of observations of the upper mesosphere and lower thermosphere over the Andes Lidar Observatory (version 2.0) [Dataset]. Zenodo. https://doi.org/10.5281/zenodo.8136987

Hecht, J. H., Walterscheid, R. L., Fritts, D. C., Isler, J. R., Senft, D. C., Gardner, C. S., & Franke, S. J. (1997). Wave breaking signatures in OH airglow and sodium densities and temperatures: 1. Airglow imaging, Na lidar, and MF radar observations. *Journal of Geophysical Research*, *102*(D6), 6655–6668. https://doi.org/10.1029/96JD02619

Hecht, J. H., Wan, K., Gelinas, L. J., Fritts, D. C., Walterscheid, R. L., Rudy, R. J., et al. (2014). The life cycle of instability features measured from the Andes Lidar Observatory over Cerro Pachón on 24 March 2012. *Journal of Geophysical Research: Atmospheres*, *119*, 8872–8898. https://doi.org/10.1002/2014JD021726

Laughman, B., Fritts, D., & Werne, J. (2011). Comparisons of predicted bore evolutions by the Benjamin-Davis-Ono and Navier-Stokes equations for idealized mesopause thermal ducts. *Journal of Geophysical Research*, *116*, D02120. https://doi.org/10.1029/2010JD014409

Laughman, B., Fritts, D. C., & Werne, J. (2009). Numerical simulation of bore generation and morphology in thermal and doppler ducts. *Annales Geophysicae*, *27*(2), 511–523. https://doi.org/10.5194/angeo-27-511-2009

Lighthill, J. (1978). *Waves in fluids*. Cambridge University Press.

Liu, A. Z., Hocking, W. K., Franke, S. J., & Thayaparan, T. (2002). Comparison of Na lidar and meteor radar wind measurements at Starfire Optical Range, NM, USA. *Journal of Atmospheric and Solar-Terrestrial Physics*, *64*(1), 31–40. https://doi.org/10.1016/s1364-6826(01)00095-5

Liu, A. Z., Vargas, F., & Swenson, G. (2016). Na wind-temperature lidar data at Andes Lidar Observatory on 10/30/2016 [Dataset]. Zenodo. https://doi.org/10.5281/zenodo.6950788

Medeiros, A. F., Paulino, I., Wrasse, C. M., Fechine, J., Takahashi, H., Bageston, J. V., & Buriti, R. A. (2018). Case study of mesospheric front dissipation observed over the northeast of Brazil. *Annales Geophysicae*, *36*(2), 311–319. https://doi.org/10.5194/angeo-36-311-2018

Mondal, S., Sivakandan, M., Sarkhel, S., Sunil Krishna, M., Mlynczak, M. G., Russell, J. M., & Bharti, G. (2021). A case study of a thermally ducted undular mesospheric bore accompanied by ripples over the western Himalayan region. *Advances in Space Research*, *68*(3), 1425–1440. https://doi.org/10.1016/j.asr.2021.03.026

Nielsen, K., Taylor, M. J., Stockwell, R. G., & Jarvis, M. J. (2006). An unusual mesospheric bore event observed at high latitudes over Antarctica. *Geophysical Research Letters*, *33*, L07803. https://doi.org/10.1029/2005GL025649

Orlanski, I., & Bryan, K. (1969). Formation of the thermocline step structure by large-amplitude internal gravity waves. *Journal of Geophysical Research*, *74*(28), 6975–6983. https://doi.org/10.1029/JC074i028p06975

Richardson, L. F., & Shaw, W. N. (1920). The supply of energy from and to atmospheric eddies. *Proceedings of the Royal Society of London-Series A: Containing Papers of a Mathematical and Physical Character*, *97*(686), 354–373. https://doi.org/10.1098/rspa.1920.0039

Schubert, G., Walterscheid, R. L., & Hickey, M. P. (1991). Gravity wave-driven fluctuations in OH nightglow from an extended, dissipative emission region. *Journal of Geophysical Research*, *96*(A8), 13869–13880. https://doi.org/10.1029/91JA00562

Seyler, C. E. (2005). Internal waves and undular bores in mesospheric inversion layers. *Journal of Geophysical Research*, *110*, D09S05. https://doi.org/10.1029/2004JD004685

She, C. Y., Li, T., Williams, B. P., Yuan, T., & Picard, R. H. (2004). Concurrent OH imager and sodium temperature/wind lidar observation of a mesopause region undular bore event over fort Collins/Platteville, Colorado. *Journal of Geophysical Research*, *109*, D22107. https://doi.org/10.1029/2004JD004742

Shiokawa, K., Suzuki, S., Otsuka, Y., Ogawa, T., Nakamura, T., Mlynczak, M. G., & James, M. R., III. (2006). A multi-instrument measurement of a mesospheric front-like at the equator structure. *Journal of the Meteorological Society of Japanese Series II*, *84A*, 305–316. https://doi.org/10.2151/jmsj.84A.305

Smith, S. M. (2014). The identification of mesospheric frontal gravity-wave events at a mid-latitude site. *Advances in Space Research*, *54*(3), 417–424. https://doi.org/10.1016/j.asr.2013.08.014

Smith, S. M., Friedman, J., Raizada, S., Tepley, C., Baumgardner, J., & Mendillo, M. (2005). Evidence of mesospheric bore formation from a breaking gravity wave event: Simultaneous imaging and lidar measurements. *Journal of Atmospheric and Solar-Terrestrial Physics*, *67*(4), 345–356. https://doi.org/10.1016/j.jastp.2004.11.008

Smith, S. M., Stober, G., Jacobi, C., Chau, J. L., Gerding, M., Mlynczak, M. G., et al. (2017). Characterization of a double mesospheric bore over Europe. *Journal of Geophysical Research: Space Physics*, *122*, 9738–9750. https://doi.org/10.1002/2017JA024225

Smith, S. M., Taylor, M. J., Swenson, G. R., She, C.-Y., Hocking, W., Baumgardner, J., & Mendillo, M. (2003). A multidiagnostic investigation of the mesospheric bore phenomenon. *Journal of Geophysical Research*, *108*(A2), 1083. https://doi.org/10.1029/2002JA009500

Snively, J. B., Pasko, V. P., & Taylor, M. J. (2010). OH and OI airglow layer modulation by ducted short-period gravity waves: Effects of trapping altitude. *Journal of Geophysical Research*, *115*, A11311. https://doi.org/10.1029/2009JA015236

Sonmor, L. J., & Klaassen, G. P. (1997). Toward a unified theory of gravity wave stability. *Journal of the Atmospheric Sciences*, *54*(22), 2655–2680. https://doi.org/10.1175/1520-0469(1997)054⟨2655:TAUTOG⟩2.0.CO;2

Stockwell, R. G., Taylor, M. J., Nielsen, K., & Jarvis, M. J. (2011). The evolution of a breaking mesospheric bore wave packet. *Journal of Geophysical Research*, *116*, D19102. https://doi.org/10.1029/2010JD015321

Swenson, G. R., & Gardner, C. S. (1998). Analytical models for the responses of the mesospheric OH* and Na layers to atmospheric gravity waves. *Journal of Geophysical Research*, *103*(D6), 6271–6294. https://doi.org/10.1029/97JD02985

Swenson, G. R., Qian, J., Plane, J. M. C., Espy, P. J., Taylor, M. J., Turnbull, D. N., & Lowe, R. P. (1998). Dynamical and chemical aspects of the mesospheric Na "wall" event on October 9, 1993 during the airborne lidar and observations of Hawaiian airglow (ALOHA) campaign. *Journal of Geophysical Research*, *103*(D6), 6361–6380. https://doi.org/10.1029/97JD03379

Taylor, M. J., Turnbull, D. N., & Lowe, R. P. (1995). Spectrometric and imaging measurements of a spectacular gravity wave event observed during the ALOHA-93 campaign. *Geophysical Research Letters*, *22*(20), 2849–2852. https://doi.org/10.1029/95GL02948

Vargas, F., Fuentes, J., Vega, P., Navarro, L., & Swenson, G. (2020). Probing the analytical cancellation factor of short scale gravity waves using Na lidar and nightglow data from the Andes Lidar Observatory. *Atmosphere*, *11*(12), 1311. https://doi.org/10.3390/atmos11121311

Walterscheid, R. L., Gelinas, L. J., Hecht, J. H., & Liu, A. Z. (2013). Instability structures during periods of large Richardson number ($Ri > 1/4$): Evidence of parametric instability. *Journal of Geophysical Research: Atmospheres*, *118*, 6929–6939. https://doi.org/10.1002/jgrd.50514

Walterscheid, R. L., Hecht, J. H., Gelinas, L. J., Hickey, M. P., & Reid, I. M. (2012). An intense traveling airglow front in the upper mesosphere-lower thermosphere with characteristics of a bore observed over Alice Springs, Australia, during a strong 2 day wave episode. *Journal of Geophysical Research*, *117*, D22105. 10.1029/2012JD017847

Walterscheid, R. L., & Hickey, M. P. (2009). Gravity wave ducting in the upper mesosphere and lower thermosphere duct system. *Journal of Geophysical Research*, *114*, D19109. https://doi.org/10.1029/2008JD011269

Walterscheid, R. L., & Schubert, G. (1990). Nonlinear evolution of an upward propagating gravity-wave—Overturning, convection, transience and turbulence. *Journal of the Atmospheric Sciences*, *47*(1), 101–125. https://doi.org/10.1175/1520-0469(1990)047⟨0101:NEOAUP⟩2.0.CO;2

Walterscheid, R. L., Schubert, G., & Straus, J. M. (1987). A dynamical-chemical model of wave-driven fluctuations in the OH nightglow. *Journal of Geophysical Research*, *92*(A2), 1241–1254. https://doi.org/10.1029/JA092iA02p01241

Yue, J., She, C.-Y., Nakamura, T., Harrell, S., & Yuan, T. (2010). Mesospheric bore formation from large-scale gravity wave perturbations observed by collocated all-sky OH imager and sodium lidar. *Journal of Atmospheric and Solar-Terrestrial Physics*, *72*(1), 7–18. https://doi.org/10.1016/j.jastp.2009.10.002